Supporting Information for

High-throughput and Data-Driven Search for Stable Optoelectronic $AMSe_3$ Materials

Nikhil Singh,[1, #] Kushal Samanta,[2, #] Suneet K. Maharana,[3] Koushik Pal[4], Sergei Tretiak[5], Anjana Talapatra[6], Dibyajyoti Ghosh[1,2]

[1]*Department of Chemistry, Indian Institute of Technology, Delhi, Hauz Khas, New Delhi 110016, India*

[2]*Department of Materials Science and Engineering, Indian Institute of Technology, Delhi, Hauz Khas, New Delhi 110016, India*

[3]*Department of Chemistry, Indian Institute of Technology Kanpur, Kanpur, UP 208016, India*

[4]*Department of Physics, Indian Institute of Technology Kanpur, Kanpur 208016, India*

[5]*Theoretical Division and Center for Integrated Nanotechnologies, Los Alamos National Laboratory, Los Alamos, New Mexico 87545, United States*

[6]*Materials Science and Technology Division, Los Alamos National Laboratory, Los Alamos, NM, 87544, USA*

#: These authors contributed equally

Section S1: Computational Methods:

(a)DFT details:

(i) The convex hull distance: This quantity denotes the stability upon decomposition into any binary and ternary competing phases, according to the chemical reaction: $E_{hull} = E_f$ (predicted phase) – E_f (competing phases). E_{hull} is calculated using the PYMATGEN[1] library, which aggregates the PBE energies of the competing phases available on the Materials Project.[2]

(ii) Formation energy: The formula used to calculate the formation energy of $AMSe_3$ is as follows: $E_{form/atom} = 1/5[E(AMSe_3) – 1 \times E(A) – 1x\ E(M) – 3\times E(Se)]$. Where $E(AMSe_3)$ is the total energy of the $AMSe_3$ compound and E(A), E(M), and E(Se) are the chemical potentials of A, M, and Se in their respective bulk states calculated using GGA-PBE. This quantity determines the stability of the $AMSe_3$ compound with respect to decomposition to elemental states of A, M, and Se.

The reported formation energies and energy-above-hull values are based on data obtained from the Materials Project, which employs the Perdew-Burke-Ernzerhof (PBE) exchange-correlation functional within the generalized gradient approximation (GGA). It should be noted that the energy data for many competing phases of metal selenides are unavailable in this database. Consequently, computing formation energies and hull stabilities at the HSE06 level is not feasible due to the significant computational cost involved.

(iii) Effective Mass calculation: Effective mass calculations were conducted using PBE functional to analyze the electronic properties of the material. It is important to mention that although traditional GGA-PBE calculations tend to underestimate band gaps, its overall shape of electronic band structures at the GGA level is rather accurate and closely mimics the experimental results.[3]

For photovoltaic devices, high mobility of photogenerated charge carriers is essential for facilitating transport and efficient collection by electrodes. Carrier mobility is predominantly influenced by the carrier effective mass, which is calculated from the second derivatives of band structure curves near the valence band maximum (VBM, for holes) and conduction band minimum (CBM, for electrons), respectively. At the VBM and CBM in ternary selenides semiconductors, the band structure E(k) can be locally approximated as follows:

$$E(k) = E_0 + \frac{\hbar^2 k^2}{2m^*}$$

where $E(k)$ is the energy of an electron at the wavevector k in the band, E_0 is constant, describing the edge of band energy. Thus, the effective mass (m^*) can be calculated:

$$\frac{1}{m^*} = \frac{1}{\hbar^2}\frac{\partial^2 E}{\partial k_i \partial k_j}$$

We calculate the direction-dependent effective mass of carriers in the Brillouin zone of periodic lattice from one high symmetry point to another high symmetry point.

(iv) SLME determination: We calculated the selection metric for solar cell absorber, spectroscopic limited maximum efficiency (SLME) formulated by Yu and Zunger.[4] The SLME is the theoretical ratio of the maximum output power density and the total incident solar energy density. Established by the Shockley-Queisser (SQ) limit, the SLME method overcomes the limitations of conventional S-Q efficiency evaluations, primarily based on band gap values. The S-Q efficiency often fails to consider dipole-forbidden direct transitions in certain direct-gap materials. The SLME incorporates both the absorption coefficient and the material thickness, accounting for radiative and non-radiative recombination losses, and considers both direct and indirect band gaps. Based on Fermi's golden rule, this approach provides a more comprehensive and accurate evaluation of the photovoltaic performance potential compared to the SQ limit. These crucial parameters are derived through meticulous computation employing the hybrid HSE06 exchange and correlation functional approximation.

(v) Phase stability:

For phase stability assessment of 200 selected compounds: Initial exploration of phase stability was conducted where each element is represented at least once as A or M to ensure that all elements are considered. This results in the inclusivity of the whole chemical space relevant to our research. We utilize the crystal structure of the prototypes (mentioned in phase selection using prototypes) as templates. We substitute atomic sites with A's and M's from our

previously identified 200 ternary compounds to optimize structures, determining total energies for all compounds across different structures.

For phase stability assessment of screened compounds: To assess the phase stability, we computed the total energies of four different crystallographic phases using Density Functional Theory (DFT). A dense Monkhorst-Pack k-point grid was used for Brillouin zone sampling. Convergence criteria included electronic self-consistency to 10^{-6} eV and ionic relaxation until forces were below 0.01 eV/Å. After full structural optimization, the total energy per formula unit for each phase was calculated. The phase with the lowest energy was identified as the most stable configuration, providing insight into the thermodynamic preferences under equilibrium conditions.

(vi) Defect Calculation: Materials with deep-level states within the band gap are sensitive to point defects, whereas materials that harbour defect states inside the valence or conduction band or are situated in proximity (within $\approx k_BT$) to the band edges are deemed defect-tolerant. As defect property evaluation is a step in an elaborate material screening process, we employ computationally tractable methods that provide qualitatively correct insights. Single vacancy neutral defects (A, M, Se vacancy) were created to study the impact of point defects on the electronic structure of selected potential candidates within a large enough 2 x 2 x 2 supercell to avoid spurious defect-defect interactions. We use 6 x 3 x 2 Γ-centered Monkhorst-Pack mesh for the electronic structure calculations of both pristine and defective cells. We do not perform structural optimization for these defective simulation cells as that requires a considerable amount of computational resources. The representative calculations depict that structural optimization of defective simulation cells does not impact the overall electronic properties. Note that we only consider the neutral state of all the defects as our main objective is to identify overall defect-tolerant candidates.

(vii) Phonon Calculations: To establish the dynamic stability of screened $AMSe_3$ compounds, we performed phonon calculations using the PHONOPY[5] package that utilized a finite displacement supercell method for the calculation of forces and construction of the second-order interatomic force constant matrices from the force-displacement data. We used ([0, 3, 3], [1, 0, 1], [1, 1, 0]) supercell transformation matrix to generate relatively isotropic supercells. Each supercell of $AMSe_3$ has 120 atoms, and we used a 4 × 4 × 4 k-point mesh to calculate the forces on the atoms.

(viii) *Ab initio* Molecular Dynamics: To evaluate the structural stability of the screened materials at ambient conditions (300K), we perform *ab initio* molecular dynamics simulations considering a large 2 x 2 x 1 supercell. A canonical ensemble with a Nose-Hoover thermostat has been applied to simulate the AIMD trajectories of the $AMSe_3$ compounds. The entire molecular dynamics simulation lasted 5 ps with a time step of 1 fs.

(ix) Non Adiabatic Molecular Dynamics:

The *ab initio* NAMD simulations of charge carrier cooling, separation, and recombination are carried out using the fewest switches surface hopping (FSSH) algorithm[6] corrected for decoherence[7] to describe the slow recombination process. The evolution of the electronic subsystem is described within the time-dependent Kohn-Sham theory. We utilized 5 picoseconds of AIMD trajectories (with a 1 femtosecond timestep) for computations pertaining to nonadiabatic coupling at the Γ-point. To examine the electron-hole recombination process utilizing the Libra code,[8] we analyzed all 5000 snapshots along the trajectories and conducted 500 stochastic simulations using the DISH process for each geometry. We subsequently iterated the nonadiabatic Hamiltonian calculated over the 5 ps trajectory to model the charge recombination dynamics occurring over an extended period of 15 ps. We concentrate on electron-hole recombination across the band gap, highlighting the dynamic structural

characteristics that facilitate electron-phonon interactions and restrict carrier lifespan. The short-time linear approximation approach was used to analyze the exponential growth function and to determine the carrier recombination lifetimes of $BaZrSe_3$, $ScYSe_3$, and $SrHfSe_3$.

(b) Machine Learning Models:

The procedure for constructing and validating our machine learning algorithms to predict the thermodynamic stability of ternary selenides—covering their formation energy, distance to the convex hull, and optoelectronic band gap—involves four distinct phases: (i) Generating an in-house dataset comprising ternary selenides and relevant features to describe their target properties effectively. (ii) Feature engineering, which entails the identification of the most relevant attributes that have a strong correlation with the target properties. (iii) Selecting the optimal machine learning model among a range of potential algorithms offered by libraries like lazypredict, Magpie, and artificial neural networks based on their performance both with and without structural information from ternary selenide composite materials in different chemical composition spaces. (iv) Assessing the importance of the attributes to the ideal model and comprehending their physical connection to the target properties.

(i) **Dataset and feature generation:** To assemble the feature matrix for training our machine learning models, we utilize an extensive elemental property database containing both physical and chemical properties of elements in their atomic state, sourced from the Materials Agnostic Platform for Informatics and Exploration (MAGPIE).[9] Electronic properties such as Highest Occupied Molecular Orbital (HOMO) and Lowest Unoccupied Molecular Orbital (LUMO) energy levels are computed via Density Functional Theory (DFT), adhering to the relaxation and self-consistent field criteria mentioned earlier. Detailed descriptions of elemental features can be found in the Section S9. We augment our feature set by performing various mathematical operations—such as finding maximum, minimum, difference, weighted average, and standard

deviation—on corresponding elemental properties of elements A and B while preserving their unit dimensionality. For instance, if we possess electronegativity values for both A and B sites, we calculate their average, minimum, maximum, and std. deviation values. We also introduce novel features to capture structural attributes like the Goldschmidt tolerance factor and octahedral factor despite our non-perovskite system. We derive features for the shortest bond distances of A-Se and M-Se in the crystal structure of ASe or MSe from available sources in OQMD. Additionally, we incorporate mixing enthalpy data for elements in A-M obtained from Miedema's model for binary liquids, all of which are collected from MAGPIE. Consequently, our feature set comprises a total of 343 attributes.

(ii) **Feature engineering:** In the process of feature engineering, we adhere to the following steps: (a) If a specific column contains missing entries ≥ 10% of the total entries, we eliminate the entire feature column. (b) For the remaining feature columns, we replace them with the mean value of their respective column. (c) Any column with very low variance is removed. (d) Highly correlated features are removed from the independent feature set based on their linear and nonlinear correlations using Pearson and Spearman correlation matrices, with a threshold value set at ≥ 0.95 for both. (e) Finally, we eliminate feature columns that are redundant or irrelevant to the target feature using the Recursive Feature Elimination (RFE)[10] method. RFE identifies the most relevant features by recursively removing those with the smallest weight, as determined by an Extra Trees classifier or regressor in a classification or regression task, respectively. (f) Finally, we standardized the features to ensure uniform scaling across all features, aligning with the typical prerequisite of many machine learning models for standardized feature sets.

(iii) **Selecting the best model:** In this step, we perform two separate machine learning tasks: regression and classification. Before delving into the model selection, we first divided elements

A and M of our 920 data points into four groups: alkaline metals, alkaline earth metals, transition metals, and non-metals. So, in the matrix representation of element A × element M^T, we will have a (4×4) matrix with a total of 16 different combinations. We ensure that the data splitting into train and test is done equally from every 16 combinations in an 80/20 train/test splitting. This way, we can avoid randomly selected data points, which may leave some combinations predominantly for training, potentially resulting in poorer predictions for the test set.

(iv) **Feature importance:** Finally, using the best machine learning model, we compute the Permutation Feature Importance, which assesses the contribution of each feature to the model's statistical performance on a given tabular dataset. This method is especially valuable for non-linear or opaque estimators. It works by randomly shuffling the values of a single feature and then observing how much the model's performance decreases. We determine how much the model relies on such a feature by breaking the relationship between the feature and the target.

Importance of trained ML models:

The trained ML models reveal deep insights into the intricate relationships between structure, stability, and electronic properties of ternary selenides. These models revealed critical dependencies, such as the significant role of lattice parameters in predicting hull stability and the enhanced accuracy of ANN models in high-fidelity band gap prediction. Moreover, these trained models represent a critical step toward developing robust predictive frameworks capable of screening an expansive chemical space, including $AMSe_3$ compositions with mixed cations or extended to other chalcogenides (e.g., S/Se). Achieving this goal will require comprehensive training datasets to adequately capture the vast chemical space, and we aim to refine and expand our current ML models in future studies.

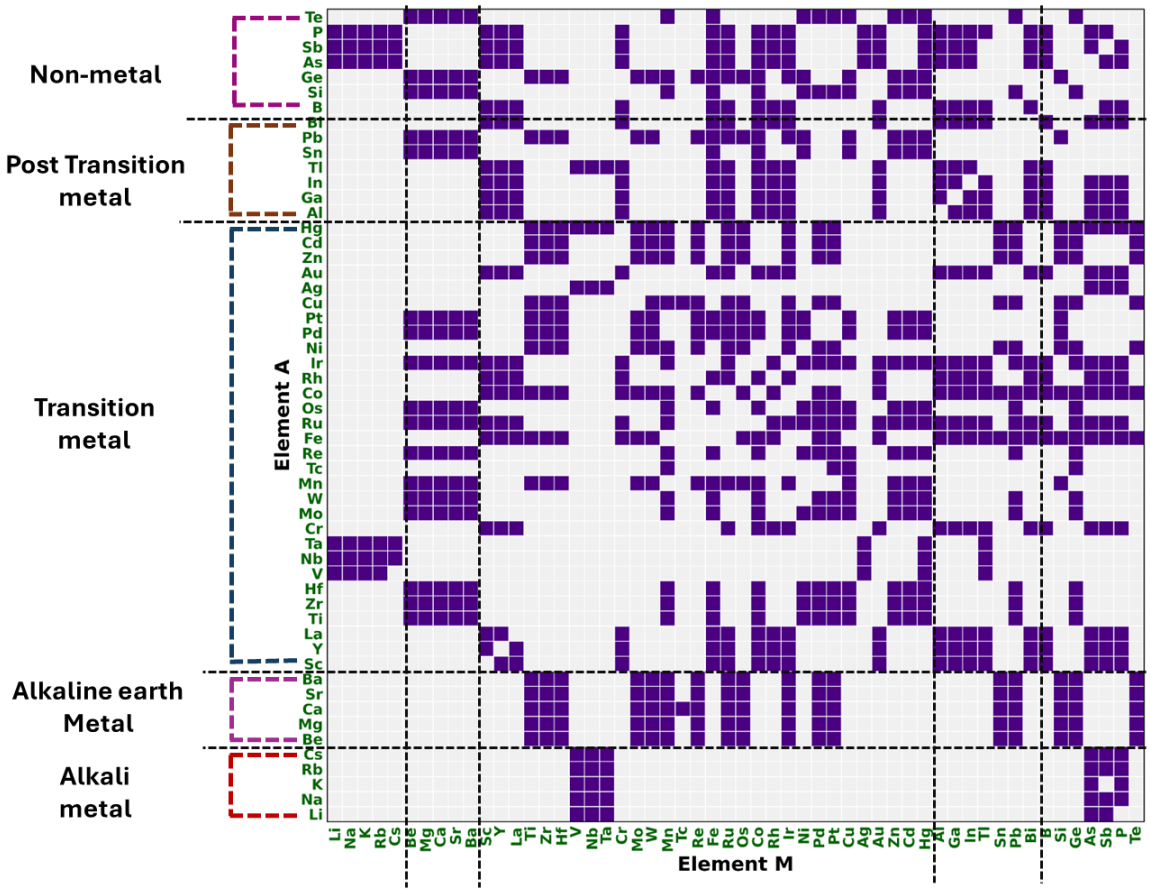

Figure S1: Composition map depicting 920 combinations of $AMSe_3$ compounds. The majority of ternary selenides consist of transition metals (~56% elements from the periodic table), while others are post-transition metals (~13%), non-metals (~13%), alkali metals (~9%), and alkaline earth metals. We have considered common oxidation states of each element for constructing the $AMSe_3$ dataset.

Table S1: Energy per atom of a subset of 200 randomly chosen compounds optimized in four different structural phases.

Energy per atom (eV) of compounds in different phases									
Compounds	$GdFeO_3$-type	NH_4CdCl_3-type	$PbPS_3$-type	$FePS_3$-type	**Compounds**	$GdFeO_3$-type	NH_4CdCl_3-type	$PbPS_3$-type	$FePS_3$-type
$AgAsSe_3$	-0.700	-0.712	-0.717	-0.711	**$MnRuSe_3$**	-1.208	-1.197	-1.146	-1.143
$AgNbSe_3$	-1.009	-1.018	-1.006	-1.015	**$MnZnSe_3$**	-0.888	-0.913	-0.876	-0.884
$AlGaSe_3$	-0.789	-0.834	-0.814	-0.820	**$MoBaSe_3$**	-1.083	-1.124	-1.123	-1.107
$AlIrSe_3$	-0.994	-1.012	-0.956	-0.964	**$NaVSe_3$**	-0.953	-0.968	-0.968	-0.961
$AlSbSe_3$	-0.799	-0.843	-0.838	-0.811	**$NbAgSe_3$**	-1.008	-1.025	-1.006	-1.020
$AlScSe_3$	-1.042	-1.051	-1.037	-1.029	**$NbKSe_3$**	-1.045	-1.044	-1.050	-1.037
$AlYSe_3$	-1.065	-1.083	-1.066	-1.052	**$NiMoSe_3$**	-1.113	-1.144	-1.144	-1.108
$AsAuSe_3$	-0.741	-0.752	-0.740	-0.726	**$NiSSe_3$**	-0.767	-0.797	-0.819	-0.799
$AsBSe_3$	-0.842	-0.872	-0.868	-0.892	**$OsBaSe_3$**	-1.060	-1.089	-1.088	-1.078
$AsCoSe_3$	-0.896	-0.898	-0.900	-0.876	**$OsCaSe_3$**	-1.036	-1.083	-1.063	-1.059
$AsKSe_3$	-0.726	-0.713	-0.744	-0.736	**$OsGeSe_3$**	-1.011	-1.066	-1.020	-1.061
$AsLiSe_3$	-0.748	-0.756	-0.760	-0.755	**$OsPtSe_3$**	-1.093	-1.100	-1.097	-1.108
$AuAlSe_3$	-0.739	-0.754	-0.760	-0.768	**$PbBeSe_3$**	-0.752	-0.776	-0.792	-0.758
$AuRhSe_3$	-0.854	-0.870	-0.818	-0.849	**$PbHgSe_3$**	-0.616	-0.616	-0.622	-0.622
$BaHfSe_3$	-1.219	-1.208	-1.198	-1.187	**$PBiSe_3$**	-0.818	-0.818	-0.827	-0.802
$BaOsSe_3$	-1.062	-1.058	-1.090	-1.057	**$PbMgSe_3$**	-0.743	-0.727	-0.748	-0.749
$BaPdSe_3$	-0.877	-0.854	-0.873	-0.873	**$PbOsSe_3$**	-1.020	-1.017	-1.027	-1.026
$BaPtSe_3$	-0.902	-0.887	-0.882	-0.901	**$PdCaSe_3$**	-0.839	-0.885	-0.870	-0.857
$BAsSe_3$	-0.829	-0.876	-0.882	-0.876	**$PdHfSe_3$**	-1.172	-1.167	-1.178	-1.169
$BaSSe_3$	-0.779	-0.798	-0.882	-0.876	**$PdMoSe_3$**	-1.094	-1.120	-1.093	-1.087
$BaWSe_3$	-1.166	-1.146	-1.188	-1.166	**$PdOsSe_3$**	-1.076	-1.079	-1.059	-1.076
$BeGeSe_3$	-0.813	-0.811	-0.809	-0.778	**$PdSiSe_3$**	-0.860	-0.884	-0.883	-0.900
$BeHfSe_3$	-1.129	-1.167	-1.137	-1.103	**$PdWSe_3$**	-1.158	-1.167	-1.165	-1.160
$BeMnSe_3$	-1.018	-1.031	-0.971	-0.959	**$PdZnSe_3$**	-0.709	-0.729	-0.721	-0.744
$BeOsSe_3$	-1.066	-1.051	-1.018	-1.011	**$PGaSe_3$**	-0.781	-0.800	-0.796	-0.782
$BePtSe_3$	-0.876	-0.895	-0.885	-0.841	**$PIrSe_3$**	-0.989	-1.019	-0.986	-0.966
$BeReSe_3$	-1.097	-1.097	-1.093	-1.075	**$PKSe_3$**	-0.767	-0.743	-0.770	-0.780
$BeSiSe_3$	-0.819	-0.863	-0.857	-0.829	**$PRbSe_3$**	-0.764	-0.735	-0.757	-0.777
$BeTiSe_3$	-1.027	-1.058	-1.023	-1.001	**$PtBeSe_3$**	-0.829	-0.888	-0.856	-0.888
$BeWSe_3$	-1.122	-1.165	-1.110	-1.108	**$PtCoSe_3$**	-0.964	-0.983	-0.958	-0.993
$BeZrSe_3$	-1.074	-1.110	-1.091	-1.052	**$PtHgSe_3$**	-0.656	-0.725	-0.684	-0.724
$BFeSe_3$	-1.017	-1.023	-0.992	-1.004	**$PtMgSe_3$**	-0.789	-0.854	-0.843	-0.836
$BiBSe_3$	-0.818	-0.851	-0.877	-0.873	**$PtNiSe_3$**	-0.914	-0.939	-0.918	-0.946
$BiCoSe_3$	-0.889	-0.884	-0.865	-0.862	**$PtReSe_3$**	-1.149	-1.172	-1.158	-1.165
$BiGaSe_3$	-0.759	-0.791	-0.771	-0.781	**$RbAsSe_3$**	-0.701	-0.699	-0.716	-0.723
$BiIrSe_3$	-0.962	-0.940	-0.929	-0.924	**$RbPSe_3$**	-0.711	-0.735	-0.770	-0.757
$BiTlSe_3$	-0.700	-0.721	-0.705	-0.715	**$RbSbSe_3$**	-0.698	-0.704	-0.725	-0.719
$BiYSe_3$	-1.046	-1.052	-1.022	-1.019	**$RbTaSe_3$**	-1.085	-1.107	-1.101	-1.092
$CaGeSe_3$	-0.827	-0.862	-0.845	-0.839	**$ReBeSe_3$**	-1.062	-1.129	-1.062	-1.122
$CaMoSe_3$	-1.103	-1.101	-1.089	-1.086	**$ReCdSe_3$**	-0.950	-1.004	-0.977	-0.989
$CaRuSe_3$	-1.018	-1.031	-1.000	-0.990	**$ReCuSe_3$**	-1.068	-1.097	-1.070	-1.090
$CaSnSe_3$	-0.837	-0.838	-0.838	-0.841	**$ReZnSe_3$**	-0.969	-1.011	-0.968	-0.997
$CaTcSe_3$	-1.067	-1.068	-1.071	-1.066	**$RhAuSe_3$**	-0.848	-0.877	-0.857	-0.879
$CaTiSe_3$	-1.090	-1.089	-1.067	-1.065	**$RhCoSe_3$**	-1.033	-1.044	-1.055	-1.045
$CdGeSe_3$	-0.666	-0.675	-0.705	-0.681	**$RhCrSe_3$**	-1.134	-1.168	-1.152	-1.152
$CdPdSe_3$	-0.702	-0.718	-0.721	-0.706	**$RhGaSe_3$**	-0.871	-0.938	-0.889	-0.929
$CdReSe_3$	-0.965	-0.997	-0.978	-0.984	**$RhRuSe_3$**	-1.120	-1.128	-1.120	-1.117

$CdTeSe_3$	-0.597	-0.613	-0.610	-0.584	**$RhSbSe_3$**	-0.883	-0.950	-0.904	-0.937
$CoGaSe_3$	-0.851	-0.903	-0.880	-0.899	**$RhTlSe_3$**	-0.819	-0.868	-0.821	-0.869
$CoPbSe_3$	-0.887	-0.910	-0.894	-0.901	**$RuCrSe_3$**	-1.195	-1.217	-1.214	-1.206
$CoReSe_3$	-1.197	-1.209	-1.189	-1.200	**$RuIrSe_3$**	-1.148	-1.171	-1.137	-1.142
$CoScSe_3$	-1.085	-1.131	-1.090	-1.085	**$RuMnSe_3$**	-1.180	-1.202	-1.169	-1.182
$CoSnSe_3$	-0.891	-0.919	-0.898	-0.920	**$RuPSe_3$**	-0.974	-1.023	-0.996	-1.037
$CrBSe_3$	-1.031	-1.120	-1.063	-1.103	**$RuRhSe_3$**	-1.113	-1.121	-1.099	-1.104
$CrCoSe_3$	-1.136	-1.155	-1.108	-1.089	**$RuYSe_3$**	-1.179	-1.238	-1.215	-1.210
$CrRhSe_3$	-1.159	-1.169	-1.126	-1.092	**$SbAsSe_3$**	-0.786	-0.807	-0.798	-0.785
$CsTaSe_3$	-1.082	-1.094	-1.101	-1.106	**$SbRbSe_3$**	-0.719	-0.706	-0.731	-0.719
$CuGeSe_3$	-0.751	-0.776	-0.783	-0.773	**$SbScSe_3$**	-1.019	-1.028	-1.009	-0.997
$CuHfSe_3$	-1.107	-1.130	-1.110	-1.104	**$ScPSe_3$**	-1.025	-1.050	-1.033	-1.048
$CuPbSe_3$	-0.759	-0.764	-0.761	-0.764	**$ScSbSe_3$**	-0.999	-1.033	-1.001	-0.998
$CuSSe_3$	-0.691	-0.718	-0.744	-0.722	**$SiBeSe_3$**	-0.836	-0.853	-0.867	-0.858
$CuTcSe_3$	-1.022	-1.034	-1.001	-1.003	**$SiNiSe_3$**	-0.885	-0.920	-0.907	-0.892
$CuZrSe_3$	-1.052	-1.073	-1.061	-1.053	**$SnFeSe_3$**	-0.955	-0.962	-0.945	-0.953
$FeBSe_3$	-0.954	-1.047	-1.014	-1.053	**$SnSrSe_3$**	-0.816	-0.849	-0.817	-0.817
$FeCoSe_3$	-1.058	-1.081	-1.057	-1.064	**$SrSiSe_3$**	-0.870	-0.910	-0.902	-0.884
$GaBiSe_3$	-0.751	-0.783	-0.784	-0.750	**$SrTiSe_3$**	-1.084	-1.066	-1.079	-1.061
$GaInSe_3$	-0.727	-0.757	-0.758	-0.737	**$TaCsSe_3$**	-1.120	-1.112	-1.126	-1.106
$GaIrSe_3$	-0.939	-0.966	-0.907	-0.906	**$TaHgSe_3$**	-1.506	-0.997	-0.996	-0.995
$GaSbSe_3$	-0.746	-0.785	-0.781	-0.743	**$TaKSe_3$**	-1.121	-1.121	-1.125	-1.112
$GeCaSe_3$	-0.829	-0.846	-0.838	-0.812	**$TaTlSe_3$**	-1.079	-1.115	-1.112	-1.103
$GeCdSe_3$	-0.679	-0.674	-0.682	-0.685	**$TcCuSe_3$**	-1.010	-1.031	-1.011	-1.025
$GeCuSe_3$	-0.773	-0.778	-0.789	-0.776	**$TcGeSe_3$**	-1.014	-1.069	-1.021	-1.045
$GeHfSe_3$	-1.152	-1.168	-1.151	-1.126	**$TcMnSe_3$**	-1.222	-1.267	-1.208	-1.236
$GeMgSe_3$	-0.752	-0.752	-0.759	-0.752	**$TcPtSe_3$**	-1.090	-1.107	-1.090	-1.090
$GeMoSe_3$	-1.066	-1.105	-1.055	-1.068	**$TeBaSe_3$**	-0.775	-0.794	-0.771	-0.758
$GeTiSe_3$	-1.044	-1.058	-1.032	-1.030	**$TeCdSe_3$**	-0.611	-0.614	-0.611	-0.617
$GeZnSe_3$	-0.694	-0.693	-0.696	-0.704	**$TeMgSe_3$**	-0.692	-0.691	-0.680	-0.686
$HfCaSe_3$	-1.197	-1.204	-1.193	-1.188	**$TiCaSe_3$**	-1.090	-1.091	-1.082	-1.069
$HfGeSe_3$	-1.135	-1.180	-1.143	-1.150	**$TiCuSe_3$**	-1.011	-1.024	-1.015	-1.012
$HfSrSe_3$	-1.192	-1.205	-1.197	-1.181	**$TiGeSe_3$**	-1.048	-1.068	-1.050	-1.050
$HgPtSe_3$	-0.681	-0.719	-0.694	-0.675	**$TiHgSe_3$**	-0.859	-0.856	-0.878	-0.878
$HgReSe_3$	-0.907	-0.933	-0.926	-0.928	**$TiPdSe_3$**	-1.068	-1.098	-1.068	-1.049
$HgSnSe_3$	-0.614	-0.631	-0.632	-0.599	**$TlAlSe_3$**	-0.734	-0.755	-0.775	-0.750
$InAuSe_3$	-0.686	-0.691	-0.697	-0.680	**$TlAuSe_3$**	-0.637	-0.649	-0.666	-0.644
$InGaSe_3$	-0.719	-0.755	-0.749	-0.749	**$TlCrSe_3$**	-0.944	-0.955	-0.930	-0.927
$InPSe_3$	-0.757	-0.786	-0.783	-0.787	**$TlIrSe_3$**	-0.883	-0.910	-0.865	-0.858
$InRuSe_3$	-0.948	-0.950	-0.926	-0.937	**$TlScSe_3$**	-0.930	-0.932	-0.930	-0.932
$IrCdSe_3$	-0.812	-0.869	-0.834	-0.875	**$VCsSe_3$**	-0.963	-0.964	-0.987	-0.965
$IrHgSe_3$	-0.767	-0.823	-0.792	-0.827	**$VNaSe_3$**	-0.959	-0.973	-0.975	-0.965
$IrRhSe_3$	-1.087	-1.110	-1.066	-1.114	**$WNiSe_3$**	-1.172	-1.210	-1.176	-1.207
$IrRuSe_3$	-1.148	-1.167	-1.158	-1.156	**$WPdSe_3$**	-1.151	-1.197	-1.156	-1.174
$IrYSe_3$	-1.154	-1.237	-1.195	-1.178	**$YBiSe_3$**	-1.038	-1.055	-1.043	-1.013
$IrZnSe_3$	-0.836	-0.870	-0.842	-0.898	**$YIrSe_3$**	-1.220	-1.188	-1.200	-1.168
$KNbSe_3$	-1.020	-1.041	-1.038	-1.022	**$YPSe_3$**	-1.058	-1.065	-1.065	-1.062
$KVSe_3$	-0.944	-0.970	-0.978	-0.969	**$YRhSe_3$**	-1.182	-1.185	-1.163	-1.123
$LiAsSe_3$	-0.743	-0.757	-0.742	-0.734	**$YTlSe_3$**	-0.954	-0.969	-0.948	-0.965
$LiSbSe_3$	-0.741	-0.748	-0.746	-0.719	**$ZnMnSe_3$**	-0.911	-0.923	-0.878	-0.870
$MgHfSe_3$	-1.110	-1.117	-1.124	-1.086	**$ZnOsSe_3$**	-0.950	-0.944	-0.918	-0.923
$MgPbSe_3$	-0.742	-0.750	-0.745	-0.723	**$ZrCdSe_3$**	-0.969	-0.978	-0.962	-0.990
$MgTiSe_3$	-1.000	-0.995	-0.979	-0.988	**$ZrPtSe_3$**	-1.157	-1.173	-1.135	-1.126

Section S2: Structural parameters of $AMSe_3$ compounds:

S2.1 Previous studies involving the NH_4CdCl_3-like Orthorhombic Pnma phase

Previous studies have demonstrated the stability of the NH_4CdCl_3-like Orthorhombic Pnma phase as the most stable among the competing phases. Ong et al. performed an extensive ab initio study to assess the phase stability of $BaZrSe_3$, revealing the preference for NH_4CdCl_3-like orthorhombic phase over other competing phases.[11] Tranchitella et al. reported the experimental synthesis of a series of $Sr_{1-x}Ba_xZrSe_3$ compounds in the NH_4CdCl_3-like orthorhombic phase.[12] $SrHfSe_3$ was successfully synthesized by Moroz et al. in NH_4CdCl_3-like Orthorhombic Pnma structure.[13] Various studies have demonstrated that the synthesis of NH_4CdCl_3-like orthorhombic phases can be achieved at reduced temperatures.

S2.2 Lattice parameters of AMSe3 in NH_4CdCl_3-like phase

The lattice parameters of our 920 ternaries exhibit a non-uniform distribution (as shown in Figure S3). The lattice constant ‘c’ spans widely across a range of 13.08 Å with a mean ± average absolute deviation of 14.32 ± 1.54 Å. Following this, the lattice constant ‘b’ displays a distribution range of 8.31 Å with a mean ± average absolute deviation of 9.41 ± 0.78 Å. Conversely, the lattice constant ‘a’ exhibits a narrower distribution, spanning 2.51 Å with a mean ± average absolute deviation of 3.89 ± 0.22 Å. This non-uniformity comes from the different orientations of octahedra in various directions. Along the lattice constant ‘a’, octahedra are densely packed, sharing edges without intervening space. However, along the lattice constants ‘b’ and ‘c’, only two octahedra are connected, leaving a gap to the next replica of these connected octahedra by an average value of 9.41 Å and 14.32 Å, respectively (shown in Figure S3).

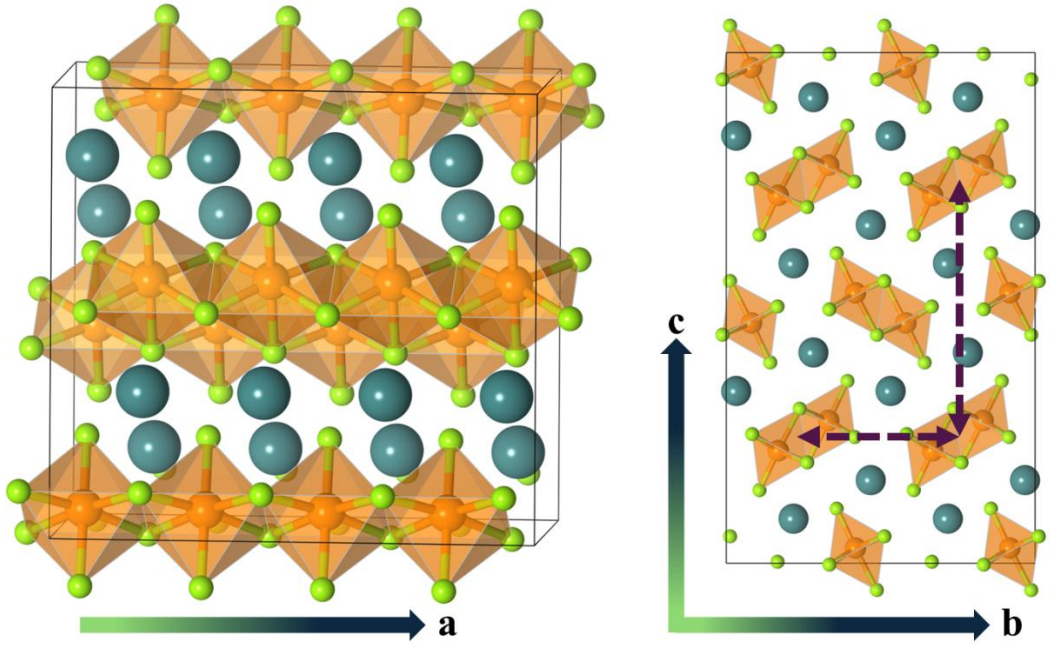

Figure S2: Schematics depicting anisotropy of lattice parameters of $AMSe_3$.

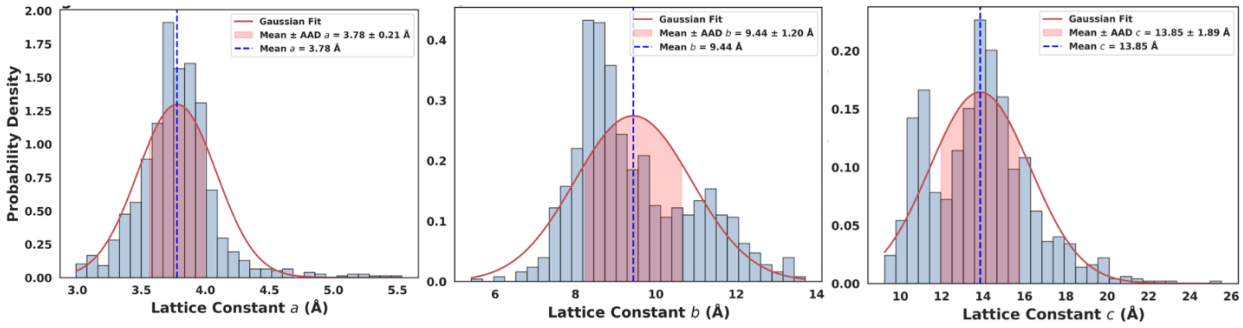

Figure S3: Distribution of lattice parameters a, b, and c for entire $AMSe_3$ dataset. The lattice parameter a has much narrower distribution than other two lattice parameters.

Section S3: Thermodynamic stability:

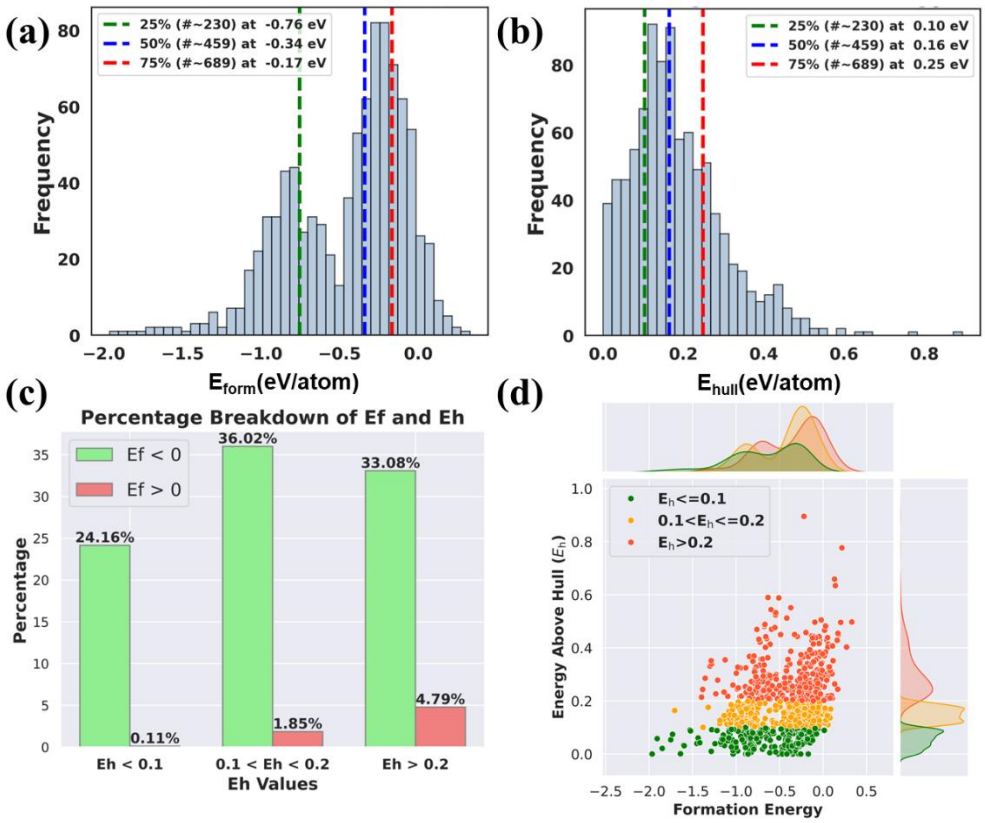

Figure S4: Distribution of (a) formation energy and (b) energy above hull values for all 920 candidates, (c) Percentage of $AMSe_3$ within certain range of hull and formation energies, (d) Scatter plot between E_h and E_f exhibiting no clear correlation between these two stability parameters.

S3.1 Formation Energy and Hull Stability: In materials science, the thermodynamic stability of a material is gauged by its hull distance (E_h), which represents the energy of decomposition. This energy (E_h) is the material's formation energy (E_f) relative to all other compounds within a defined chemical space. While E_f indicates the degree to which a compound can form from its constituent elements, the hull distance (E_h) dictates phase stability that arises from the competition among the formation energies (E_f) of all compounds within the given chemical space.

The formation energy of the materials in our dataset is predominantly less than 0 eV per atom, with 93.26% of the materials being formable ($E_f \leq 0$ eV per atom), as shown in Figures S4a d, representing the histogram and bar plot, respectively. While E_f typically ranges on the order of several eV, the E_h values are generally 1-2 orders of magnitude smaller. Additionally, the energies associated with hull distance exhibit highly nonlinear behaviour around zero (Figure S6c). Whereas E_f shows a relatively uniform distribution across a broad range of energies, with a mean ± average absolute deviation of -0.45 ± 0.31 eV per atom (Figure S4a), E_h covers a much narrower energy range, with a mean ± average absolute deviation of 0.18 ± 0.09 eV/atom (Figure S4b). We also performed the same tripartite division for the subset with $E_f > 0$ eV per atom. However, the proportion of stable and metastable candidates in this subset is insignificant, at 0.11% and 1.85%, respectively, while the unstable candidates constitute 4.79% (refer to Figure S4c).

Table S2: $AMSe_3$ candidates with $E_h = 0$ eV/atom along with their formation energy per atom in NH_4CdCl_3-type phase.

Compound	Formation energy in NH_4CdCl_3-type phase (eV/atom)	Formation energy for $AMSe_3$ as included in OQMD* (eV/atom)
$RbNbSe_3$	-0.870	
$CsNbSe_3$	-0.888	-0.832 (id:1482812)
$CaTcSe_3$	-0.870	
$SrMnSe_3$	-1.038	
$SrTeSe_3$	-0.826	-0.789 (id: 1347292)
$BaHfSe_3$	-1.643	
$BaMnSe_3$	-1.034	
$BaTeSe_3$	-0.863	
$BaZrSe_3$	-1.639	
$LaYSe_3$	-1.965	
$CrAsSe_3$	-0.325	-0.318 (id: 1733621)
$MnHgSe_3$	-0.280	
$NiMnSe_3$	-0.348	

$CuTcSe_3$	-0.171	
$HgMnSe_3$	-0.281	
$GaRhSe_3$	-0.515	
$GeMnSe_3$	-0.375	
$AsAlSe_3$	-0.477	
$SbAlSe_3$	-0.544	
$SbInSe_3$	-0.388	
$BiAlSe_3$	-0.613	
$BiAsSe_3$	-0.258	
$BiCrSe_3$	-0.465	
$BiInSe_3$	-0.469	
$BiRhSe_3$	-0.417	

*In bracket, we provide the compound ID from OQMD database.

We find that none of these compounds are documented in NH_4CdCl_3-type phase within established materials databases, such as the Materials Project and the Open Quantum Materials Database (OQMD). The phases for some of these compounds that are included in OQMD, are unstable compared to NH_4CdCl_3-type phase as shown in the 3rd column of Table S2. For the comparison of formation energy values with the OQMD entries, we have calculated them using our own parameters and have taken structure from the OQMD.

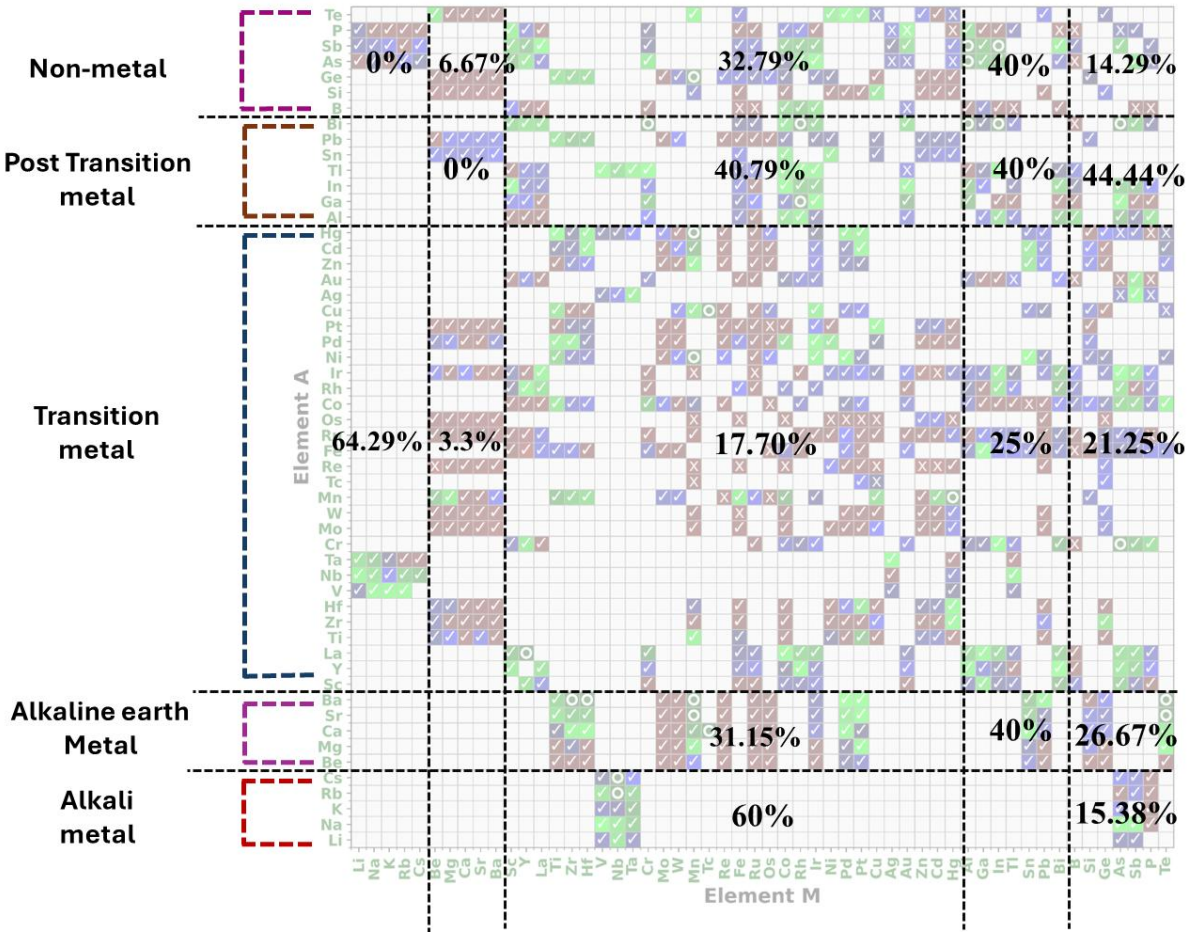

Figure S5: Percentage distribution of hull stable/metastable $AMSe_3$ compounds in each chemically distinct region.

S3.2 Experimental realization of Metastable phases of materials: Several evidence suggest that materials with a convex hull distance near zero are prime candidates for successful synthesis under experimental conditions. Metastable phases, typically challenging to synthesize, have been experimentally validated in several cases.[14] By broadening the convergence region of the convex hull to 0.1 eV/atom, metastable candidates are found to be distributed across a wide compositional range. This expanded approach aligns with the methodologies adopted in other high-throughput studies, which have similarly employed critical tolerance values for the convex hull.[15–17] The experimental methods can be fine-tuned to stabilize these promising $AMSe_3$ systems for optoelectronic applications.

Advanced experimental synthesis techniques enable the discovery of functional selenide materials beyond traditional equilibrium phases and compositions. High-temperature synthesis methods, such as those utilizing resistive-bearing furnaces[18–20] or superfast heating techniques[21], have become invaluable in this pursuit. These methods have been extensively applied to the synthesis of metastable nanomaterials, including single-atom alloys[22], high-entropy alloys,[23] and oxides.[24] The efficacy of high-temperature synthesis platforms lies in their ability to control key reaction parameters precisely. By adjusting reaction time, temperature, the choice of reactants, and atmospheric conditions, researchers can effectively navigate the synthesis of metastable compositions. This control helps to prevent undesirable phenomena such as phase separation, coarsening, and ripening, which can compromise the stability and purity of the synthesized materials. The implications of these advancements are profound. With the capability to stabilize metastable phases, a broader range of functional materials can be accessed, offering new opportunities for technological applications.

Advanced experimental synthesis techniques enable the discovery of functional selenide materials beyond traditional equilibrium phases and compositions. High-temperature synthesis methods, such as those utilizing resistive-bearing furnaces[18–20] or superfast heating techniques[21], have become invaluable in this pursuit. These methods have been extensively applied to the synthesis of metastable nanomaterials, including single-atom alloys[22], high-entropy alloys,[23] and oxides.[24] The efficacy of high-temperature synthesis platforms lies in their ability to control key reaction parameters precisely. By adjusting reaction time, temperature, the choice of reactants, and atmospheric conditions, researchers can effectively navigate the synthesis of metastable compositions. This control helps to prevent undesirable phenomena such as phase separation, coarsening, and ripening, which can compromise the stability and purity of the synthesized materials. The implications of these advancements are profound. With

the capability to stabilize metastable phases, a broader range of functional materials can be accessed, offering new opportunities for technological applications.

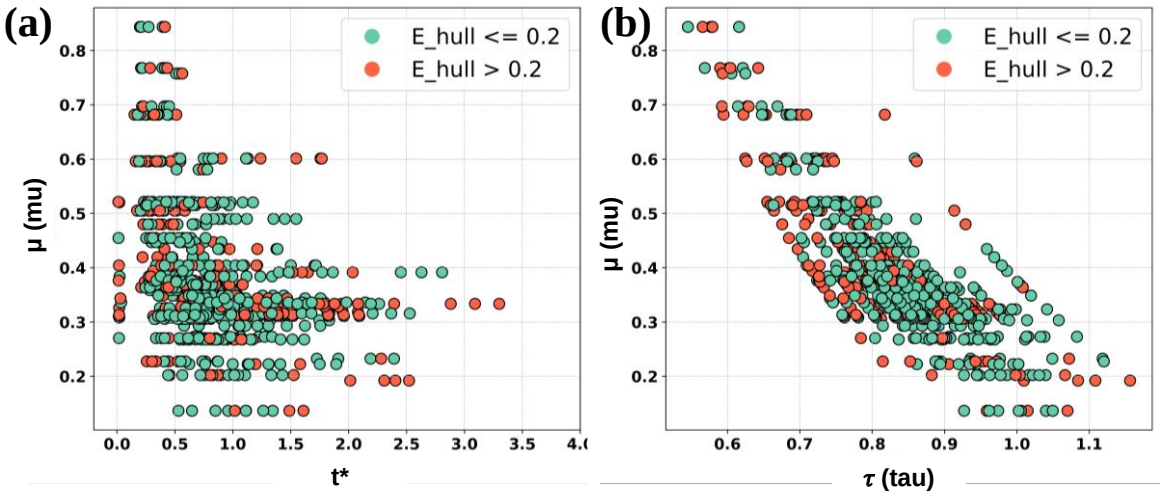

Figure S6: Scatter plot between (a) μ(octahedral factor) and t*(modified tolerance factor) and (b) μ(octahedral factor) and τ (Goldschmidt tolerance factor). These plots illustrate that traditional geometry parameters are not suitable for classifying stability/instability region of $AMSe_3$.

Section S4: Machine Learning models involving thermodynamic stability:

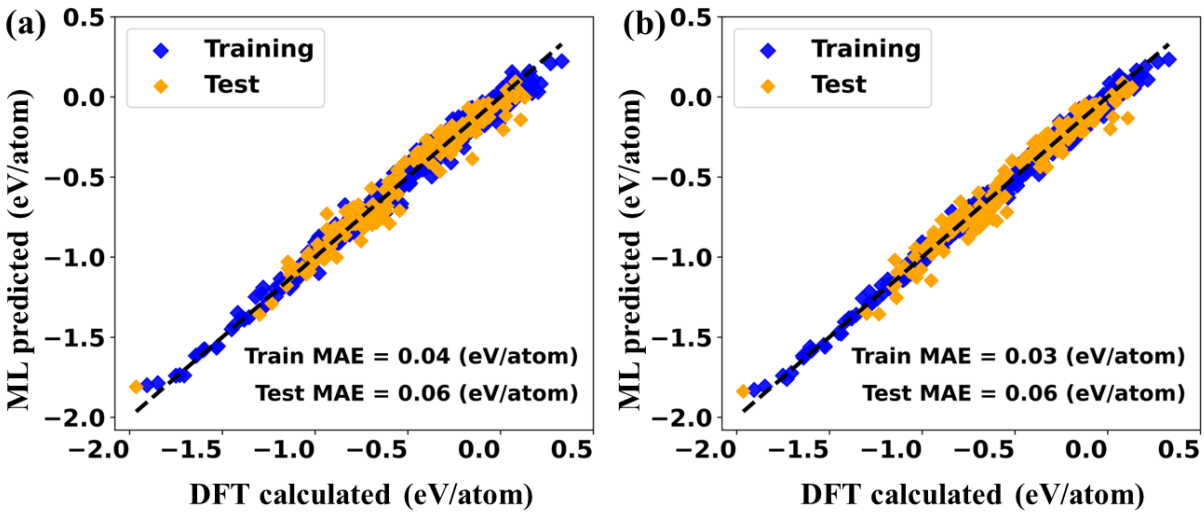

Figure S7: Prediction of E_f using (a) Hist gradient boosting regressor and (b) XGBoost regressor models. These models use elemental and compositional features for training and testing.

S4.1 Hull stability regression: Predicting the exact numerical values of the hull distances for $AMSe_3$ materials using only elemental and compositional features is challenging, as phase stability is not an intrinsic property of the materials. The best regressor model with elemental features, the gradient boosting regressor, achieves a test MAE of 0.05 eV/atom. However, when we include lattice parameters as features, the hist gradient boosting regressor model outperformed the others, reducing the test MAE to 0.04 eV/atom—a 20% improvement in accuracy.

Given the high prediction accuracy for the formation energy of the materials, we included the formation energy values as a feature to predict hull distances. Although Figure S4d shows no direct relationship between formation energy and hull distance, the BayesianRidge model successfully predicts hull distances with a test MAE of approximately 0.04 eV/atom, even without incorporating lattice parameters as features, as shown in Figure S8(a). The inclusion of lattice parameters here in feature list, however, does not improve the model accuracy any further (Figure S8b).

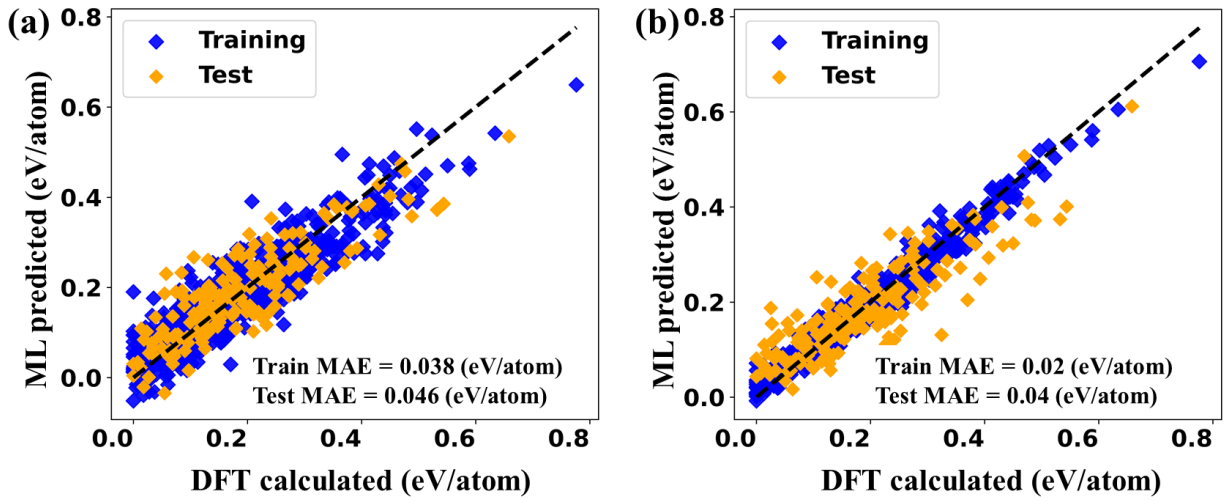

Figure S8: Prediction of E_h with hist gradient boost regressor model considering (i) E_f and elemental features (no lattice parameters included) and (ii) E_f, elemental features, and lattice parameters as features.

S4.2 Feature importance for thermodynamic stability:

We briefly discuss the significance of various features of the target properties. This analysis elucidates the contribution of each feature to the target. When the direct mathematical relationship between the target and features is unknown, the ML model identifies the importance of specific features. This insight facilitates the connection of these features to the target property, thereby enhancing our understanding of the material's physical characteristics and are extremely valuable for strategically designing stable functional materials that are yet to be realized experimentally.

Section S5: Electronic Properties

S5.1 Machine Learning models involving Bandgap prediction:

Bandgap regression: First, we utilize only elemental and compositional features to predict the numerical values of the HSE06 bandgap for ternary selenides. Training the model with this

information for bandgap prediction is challenging, as the R^2 value for the best model is approximately 70%. However, the Mean Absolute Error (MAE) is relatively low, around 0.24 eV. Various models, including hist gradient boosting regressor, LGBMRegressor, XGBRegressor, RandomForestRegressor, and ExtraTreesRegressor, perform similarly, with MAE values ranging between 0.24 and 0.26 eV.

Incorporating lattice parameters as structural features does not lead to a significant improvement in prediction accuracy. The LGBMRegressor model, for instance, achieves an MAE of 0.23 eV. Additionally, the feature importance of lattice constants is considerably lower than that of elemental features such as max_ion_ener and max_phi.

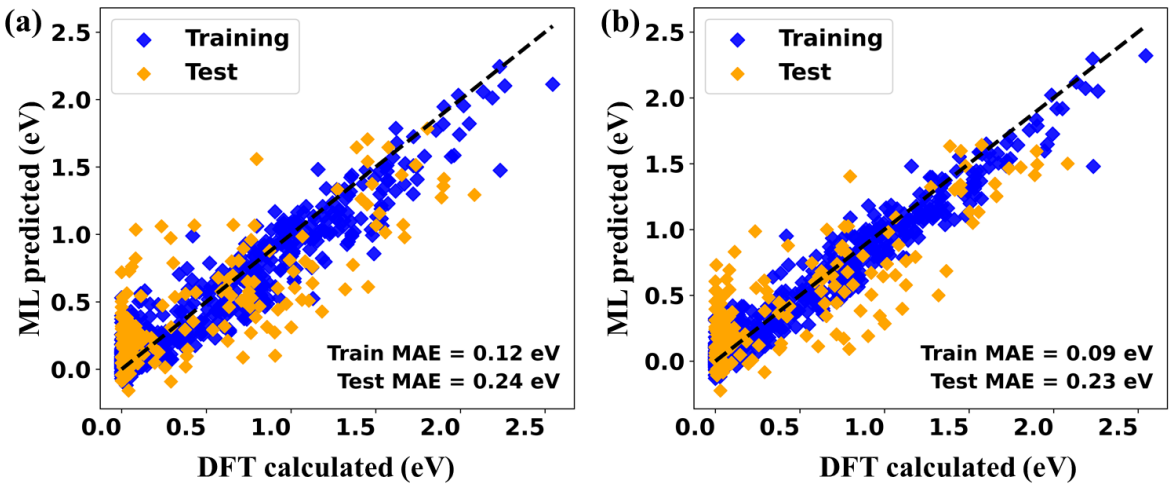

Figure S9: Bandgap prediction by using (a) elemental features only, (b) elemental and lattice parameters as features.

Examining the correlation between GGA-PBE and HSE06-level bandgap values, there is no significant correlation in the narrower bandgap region (PBE Band Gap $\leq$ 0.2 eV and HSE06 Band Gap $\leq$ 0.8 eV, as shown in Figure S11b). However, in the wider bandgap regions, a linear

relationship emerges. By including GGA-PBE bandgap values as a feature, the ANN model demonstrates improved accuracy, achieving an MAE of 0.16 eV.

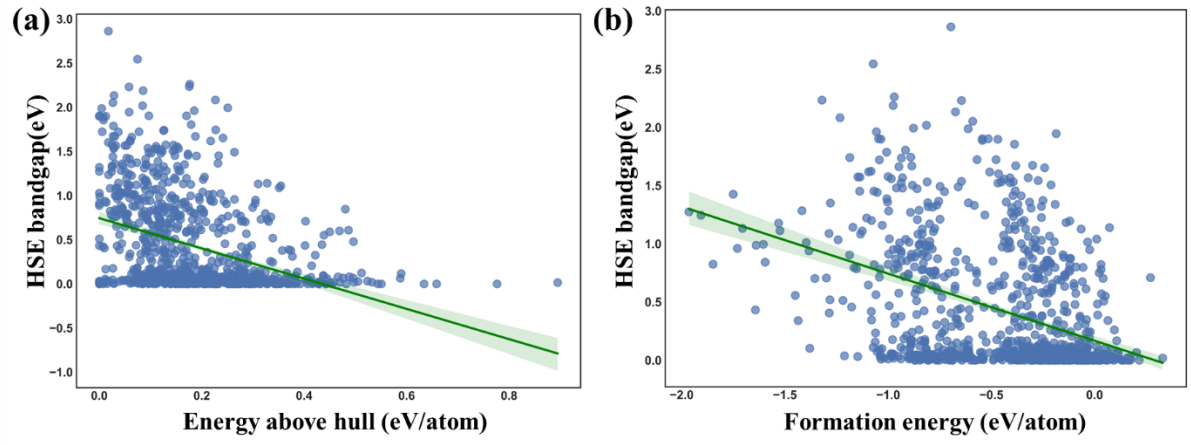

Figure S10: (a) HSE06 bandgap vs energy above hull (E_h) and (b) HSE06 bandgap and formation energy (E_f). Both E_h and E_f exhibit a negative correlation with the HSE06 bandgap.

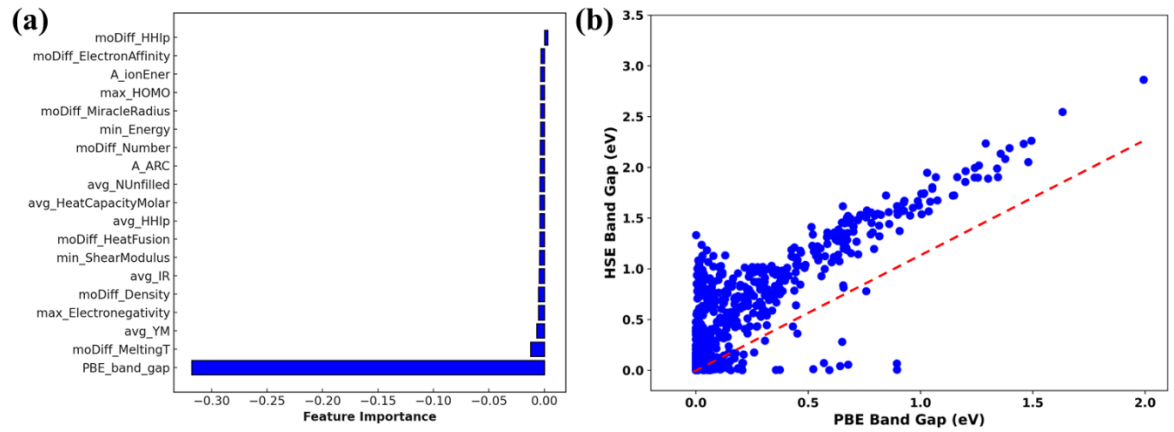

Figure S11: (a) Feature importance of ANN model when PBE bandgap is included as a feature and (b) Scatter plot between GGA-PBE and HSE06 band gaps displaying correlation.

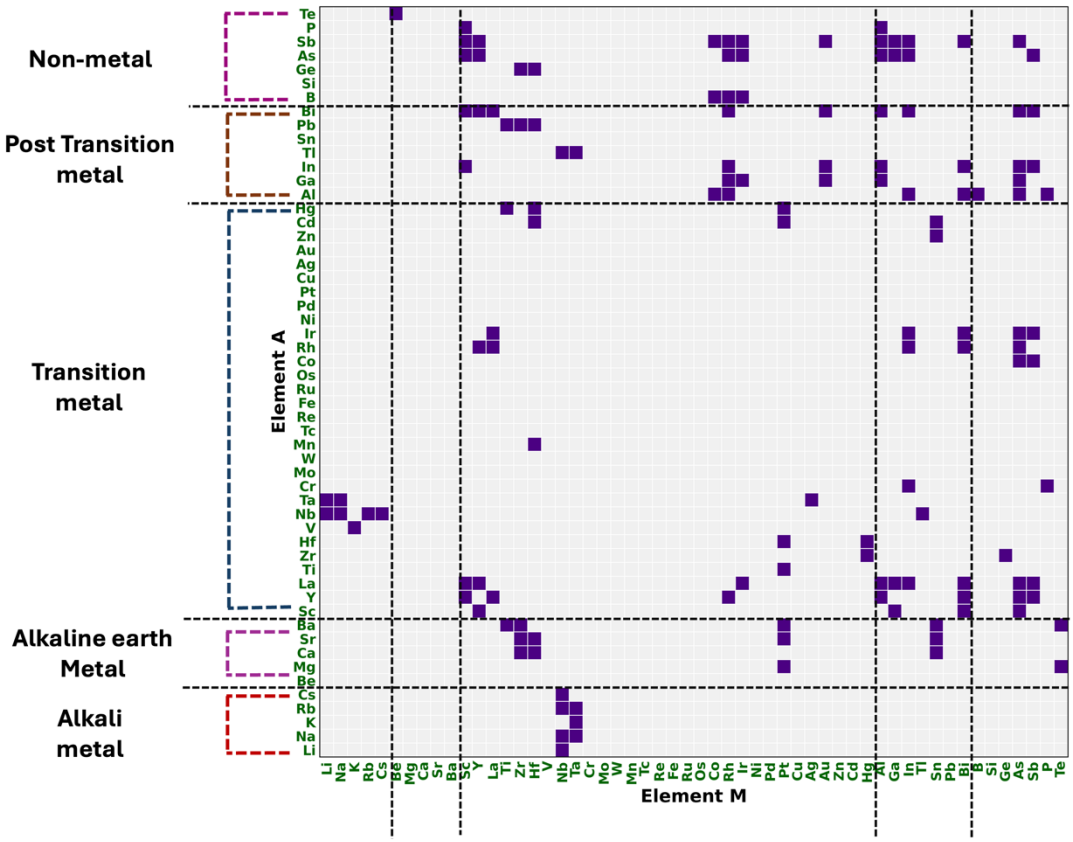

Figure S12: A/M composition map of 137 stable (E_h<0.1 eV/atom and $E_f \leq 0$ eV/atom) candidates having HSE06 bandgap > 0.5 eV.

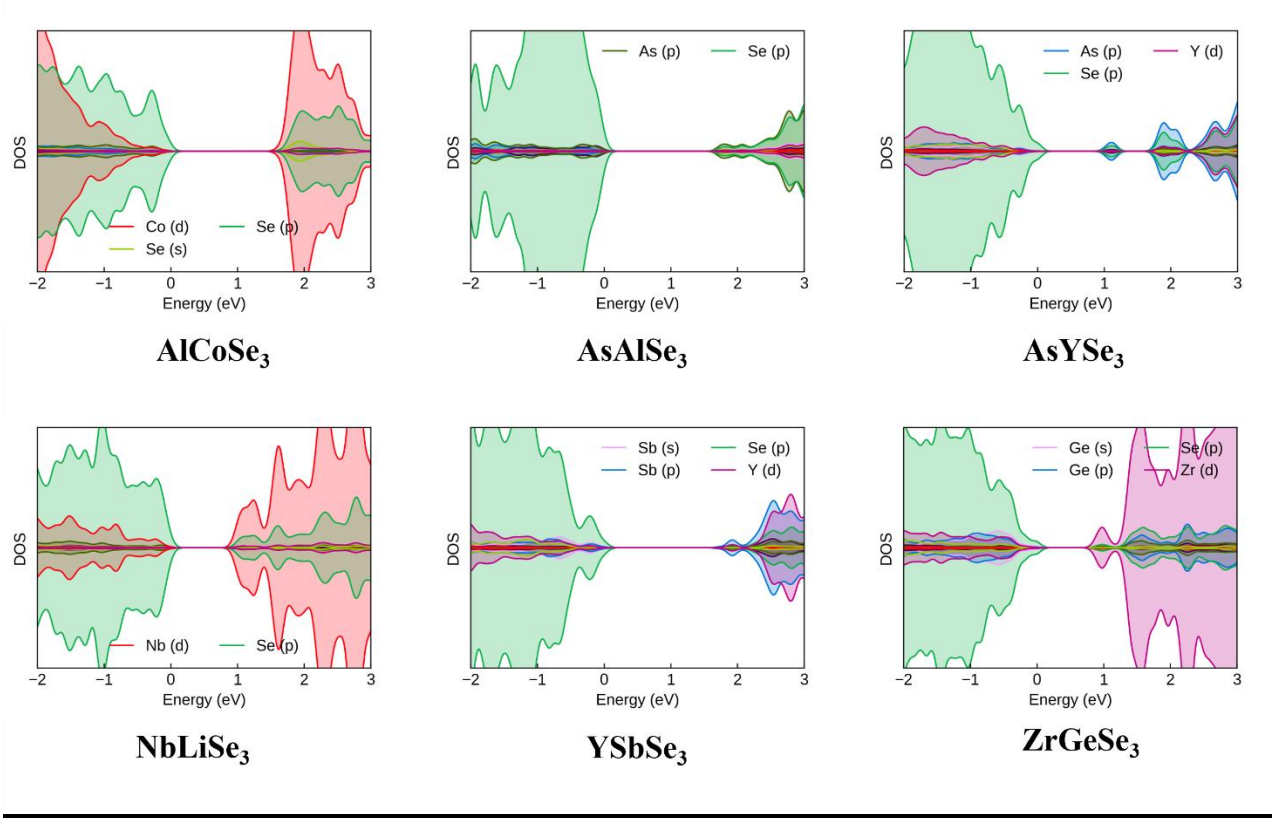

Figure S13: pDOS of a few representative $AMSe_3$ candidates.

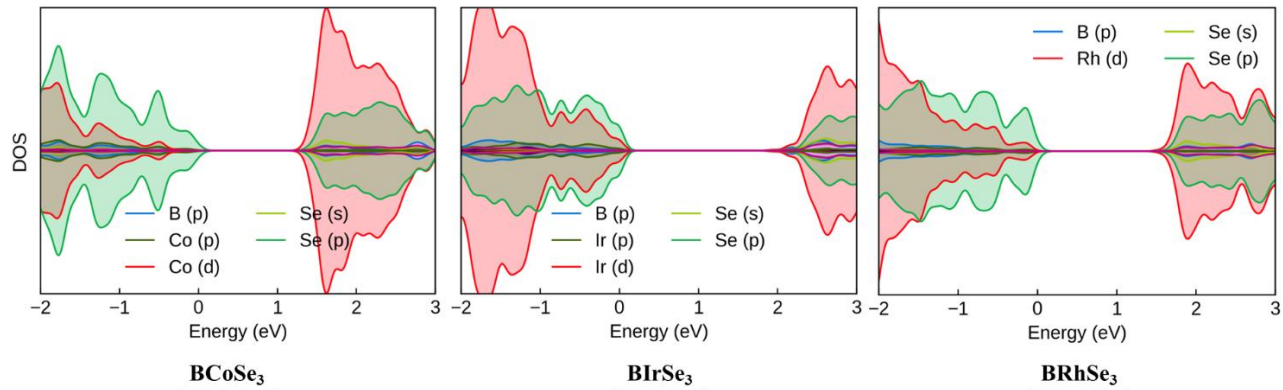

Figure S14: Projected density of state plots for $BMSe_3$ systems (M= Co, Ir, Rh).

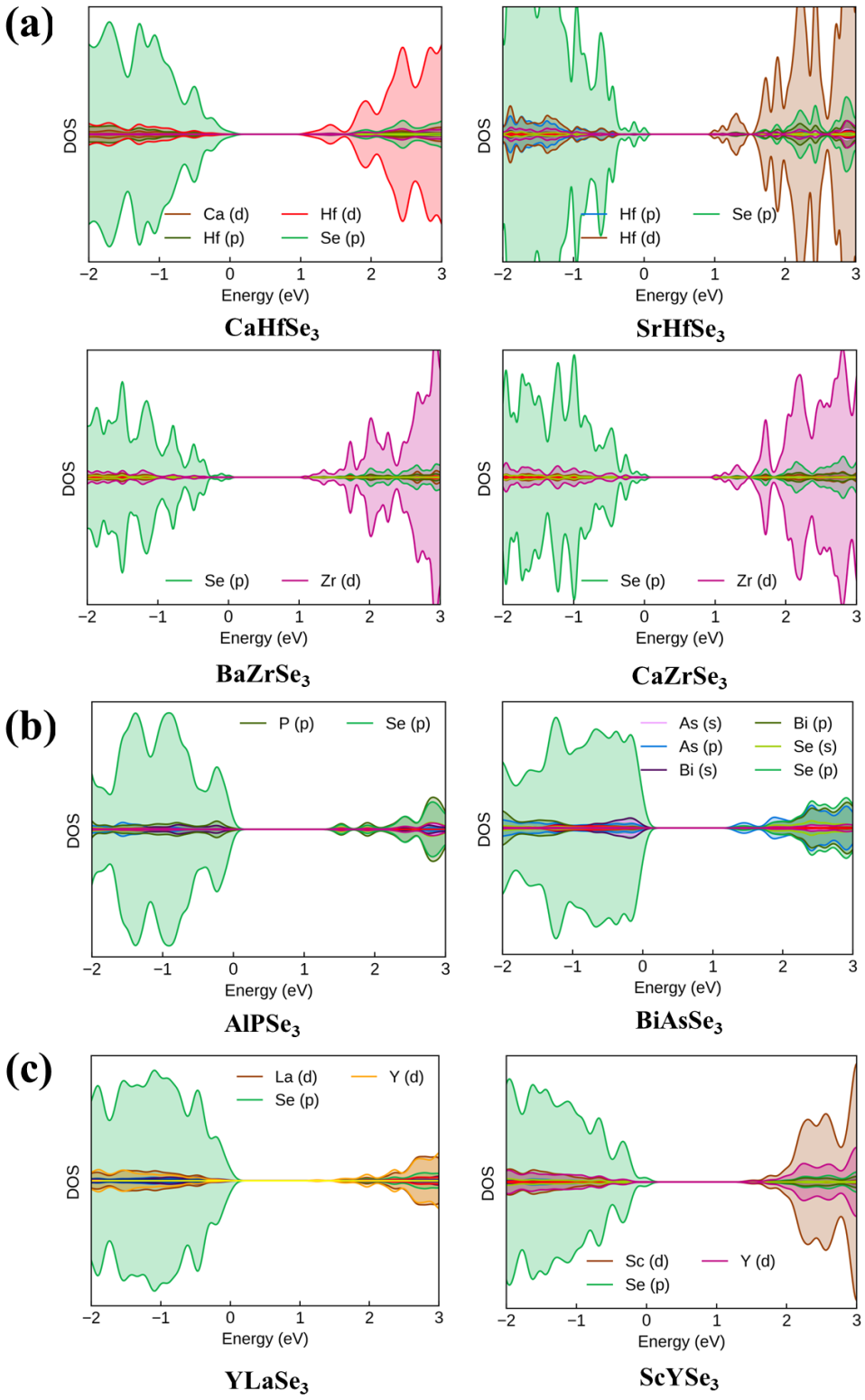

Figure S15: Density of States plot for (a) different A cations in $AMSe_3$ having M=Zr, Hf. (b) Compounds having non-metal cation as 'M'. (c) Compounds having rare earth elements at both 'A' and 'M' sites.

S5.2 Chemical Trends in Compounds with suitable direct bandgap

The screened compounds frequently contain A-site elements that include a variety of p-block (such as As, Bi, and Sb) and s-block elements (like Li, Na, and Ca), suggesting that both heavier post-transition metals and lighter alkali and alkaline earth metals can stabilize NH_4CdCl_3-phase structures with desirable electronic properties. The relatively heavy alkaline earth metals like Sr and Ba also occupy A-sites in these $AMSe_3$ compounds. However, most of these A-site elements do not contribute to the band edge states, remaining largely inert to the electronic properties of the corresponding $AMSe_3$.

The M-site elements of $AMSe_3$ display a similarly broad chemical space involving transition metals (such as Co, Rh, and Ir) and main group elements (like Al, Ga, and Ge) (Figure 4). Notably, several screened compounds include M-site elements like Zr, Hf, and Ti, which are commonly reported to form stable ternary sulfides and selenides in different phases. As M-sites form MSe_6 octahedra, large variation in elemental space suggests an inherently flexible coordination environment in these ternary compounds. Furthermore, the M-site elements significantly tune the overall electronic properties as those dominantly compose the CBM state of $AMSe_3$.

We also note that the presence of heavy metals (such as Ir and Bi) and lighter elements (such as Al and Li) in the same structure points to a potential for tunable electronic and optical properties driven by the intrinsic properties of these elements. The large mass difference in the constituent elements indicates a possible modification in the phonon spectrum and vibronic couplings, eventually boosting the excited state charge carrier dynamics in these photoactive materials.

Table S3: Comparison of band gaps of a few screened $AMSe_3$ with their values as reported in various previous work.

Compound	HSE06 Bandgap (this study)	Previous study
1. $SrHfSe_3$	1.0 eV	1.0 eV (expt.)[25]
2. $CaZrSe_3$	1.11 eV	1.0 eV (theor.)[26]
3. $BaZrSe_3$	0.99 eV	1 eV (theor.)[26]
4. $SrZrSe_3$	0.84 eV	0.86 eV(theor.)[26]
5. $CaHfSe_3$	1.18 eV	1.10 eV(theor.)[26]

Table S4: List of screened candidates having direct HSE06 Bandgap > 0.5 eV along with their hole and electron effective masses. Green- Candidates having ultralow effective charge carrier masses. Red- Candidates failing the effective mass screening criteria.

Compound	HSE06 Bandgap(eV)	m_e*	m_h*	Selected?
$AlCoSe_3$	1.62	1.184	-4.309	
$AlPSe_3$	1.41	0.364	-0.514	
$AsAlSe_3$	1.72	0.601	-0.966	
$AsRhSe_3$	0.61	0.501	-0.535	
$AsYSe_3$	1	0.364	-0.483	
$BaTiSe_3$	0.56	0.41	-0.472	
$BaZrSe_3$	0.99	0.482	-0.587	
$BCoSe_3$	1.34	0.474	-1.035	
$BiAsSe_3$	1.32	0.525	-1.325	
$BIrSe_3$	1.03	0.672	-0.78	
$BiSbSe_3$	0.79	0.205	-0.468	
$BiScSe_3$	1.36	0.346	-0.611	
$BRhSe_3$	1.54	0.461	-0.802	
$CaHfSe_3$	1.18	0.877	-0.826	
$CaZrSe_3$	1.11	0.479	-0.306	
$CdSnSe_3$	1.12	0.331	-1.891	

$CrInSe_3$	1.02	0.819	-1.547	
$GaAlSe_3$	2	1.376	-1.402	
$GaIrSe_3$	1.41	0.205	-0.696	
$GeHfSe_3$	1.04	1.357	-1.815	
$GeZrSe_3$	0.85	0.406	-0.525	
$HgHfSe_3$	2.02	0.993	-1.316	
$InRhSe_3$	0.65	0.181	-0.535	
$InSbSe_3$	1.34	0.217	-0.387	
$IrLaSe_3$	1.2	1.02	-1.523	
$LaIrSe_3$	1.08	0.58	-3.001	
$LaScSe_3$	0.82	0.531	-0.656	
$LiNbSe_3$	0.66	1.41	-2.078	
$MgTeSe_3$	1.12	0.346	-0.291	
$MnMgSe_3$	1.07	0.741	-0.432	
$NaNbSe_3$	0.63	1.432	-0.967	
$NaTaSe_3$	0.76	0.978	-0.994	
$NbLiSe_3$	0.97	1.412	-3.327	
$NbNaSe_3$	1.1	1.458	-0.713	
$PAlSe_3$	1.27	1.022	-0.678	
$PbTiSe_3$	1.02	7.69	-0.503	
$PScSe_3$	0.89	7.16	-1.359	
$RhAsSe_3$	0.97	0.637	-0.642	
$RhLaSe_3$	0.79	0.852	-0.39	
$RhYSe_3$	0.82	1.283	-0.879	
$ScGaSe_3$	2.54	0.548	-1.397	
$ScYSe_3$	1.43	0.569	-0.639	
$SrHfSe_3$	1	0.401	-0.536	
$SrZrSe_3$	0.84	0.968	-0.558	
$TlTaSe_3$	0.51	1.601	-1.659	
$YLaSe_3$	1.25	0.364	-0.483	
$YRhSe_3$	0.56	0.476	-0.641	
$YSbSe_3$	1.72	0.363	-0.485	
$YScSe_3$	0.96	0.679	-0.63	
$ZrGeSe_3$	0.88	10.904	-0.511	

Optoelectronic performance:

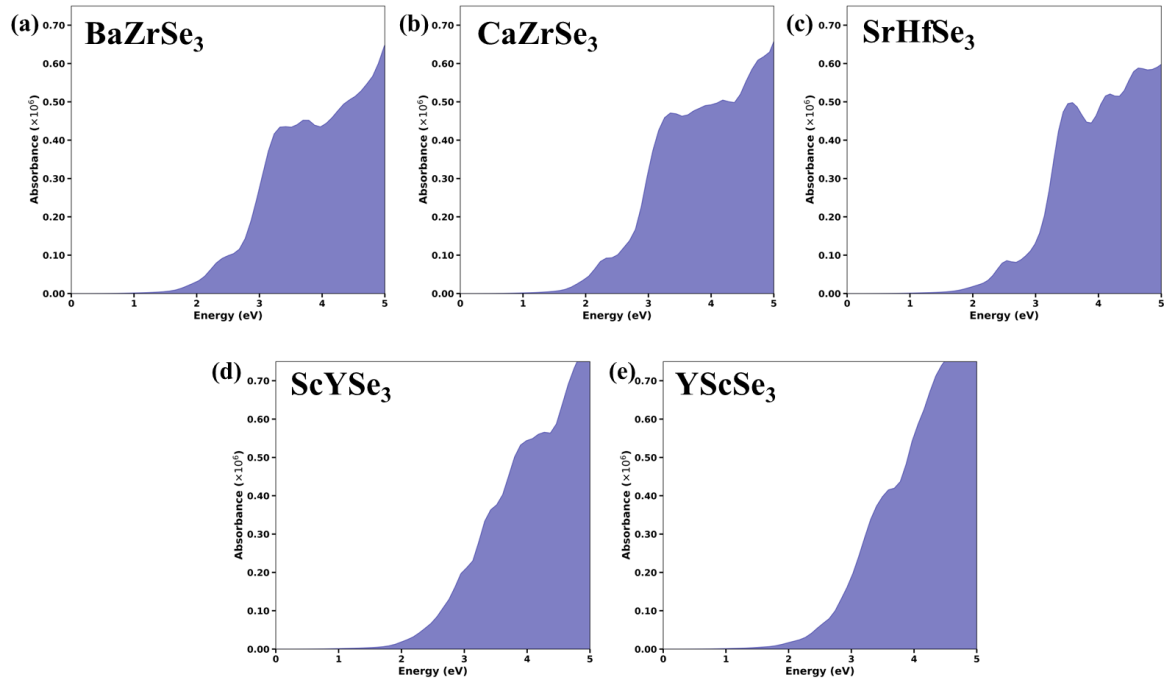

Figure S16: Absorption spectra of a few candidates with high SLME values. The sharp increase in adsorption coefficient at the band edge indicates high power conversion efficiency of these absorber materials.

Phase stability of screened materials

Table S5: Phase stability investigation of compounds having ultralow carrier effective masses. Orthorhombic $Pna2_1$ structure with corner-shared octahedra emerges as the most common competing phase for NH_4CdCl_3-like Orthorhombic Pnma compounds. The green coloured phase is the most stable one.

Compound	Total Energy of compound (in eV)			
	Monoclinic P1c1	NH_4CdCl_3-Orthorhombic Pnma	Monoclinic C12m	Orthorhombic $Pna2_1$
$BaZrSe_3$	-113.06	-116.54	-111.57	-116.52
$BiScSe_3$	-99.69	-102.26	-99.9	-102.25
$BRhSe_3$	-99.57	-98.7	-99.74	-98.7
$CaHfSe_3$	-116.73	-120.37	-116.76	-120.37
$CaZrSe_3$	-111.55	-115.93	-111.54	-114.94
$GaIrSe_3$	-89.7	-93.43	-90.16	-95.65
$GeHfSe_3$	-113.29	-115.22	-112.26	-115.21
$GeZrSe_3$	-107.8	-109.92	-107.5	-109.22
$InRhSe_3$	-83.88	-88.03	-84.24	-89.01
$MgTeSe_3$	-69.14	-67.4	-67.5	-69.48
$NaTaSe_3$	-109.05	-109.53	-108.56	-109.4
$ScYSe_3$	-58.2	-125.95	-124.96	-125.92
$SrHfSe_3$	-116.37	-120.14	-115.2	-120.14
$SrZrSe_3$	-113.89	-114.75	-111.11	-114.75
$YScSe_3$	-125.72	-128.44	-125.29	-128.44
$InSbSe_3$	-65.9	-79.42	-66.6	-76.1
$AlPSe_3$	-80.38	-82.38	-84.33	-85.88

Defect tolerance:

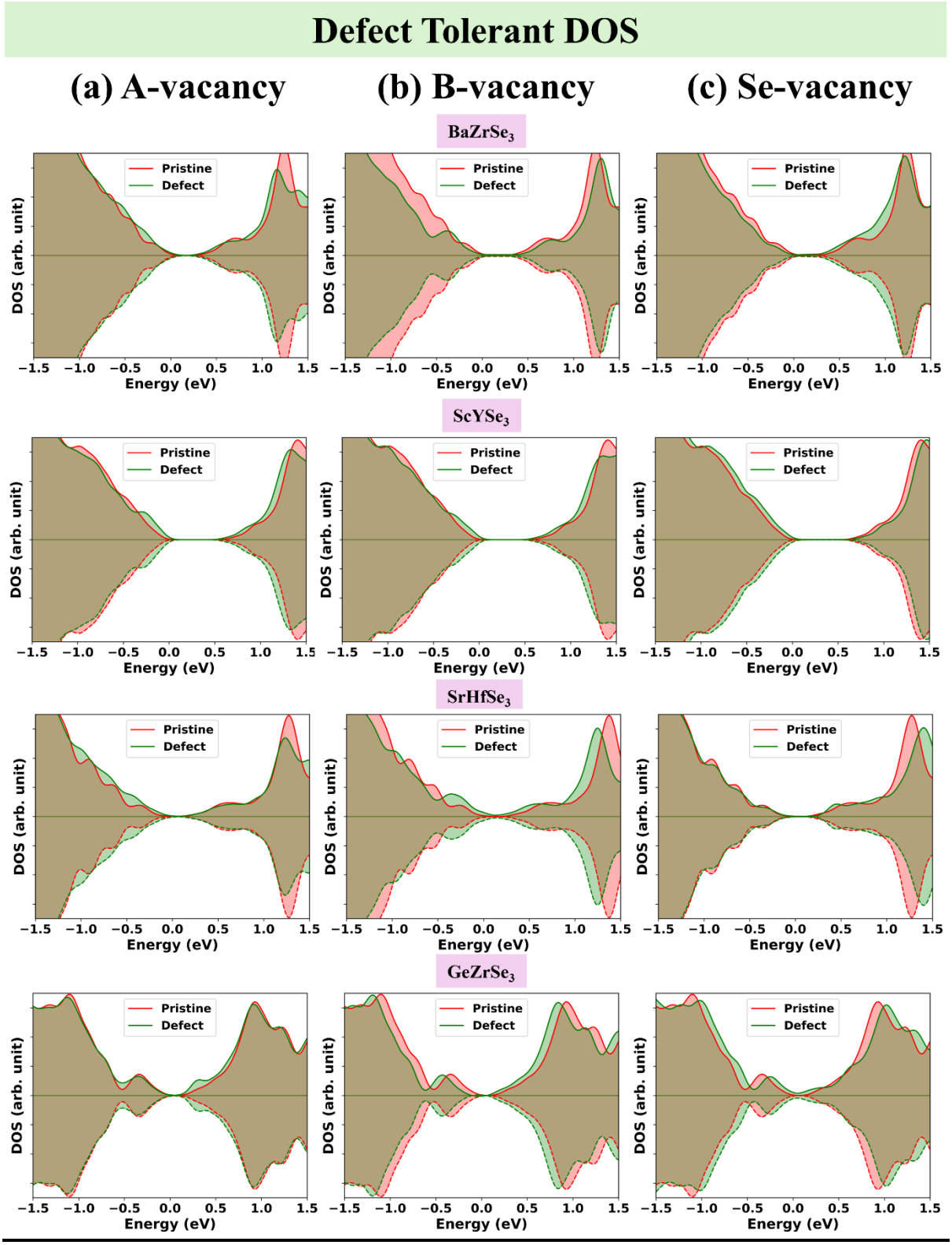

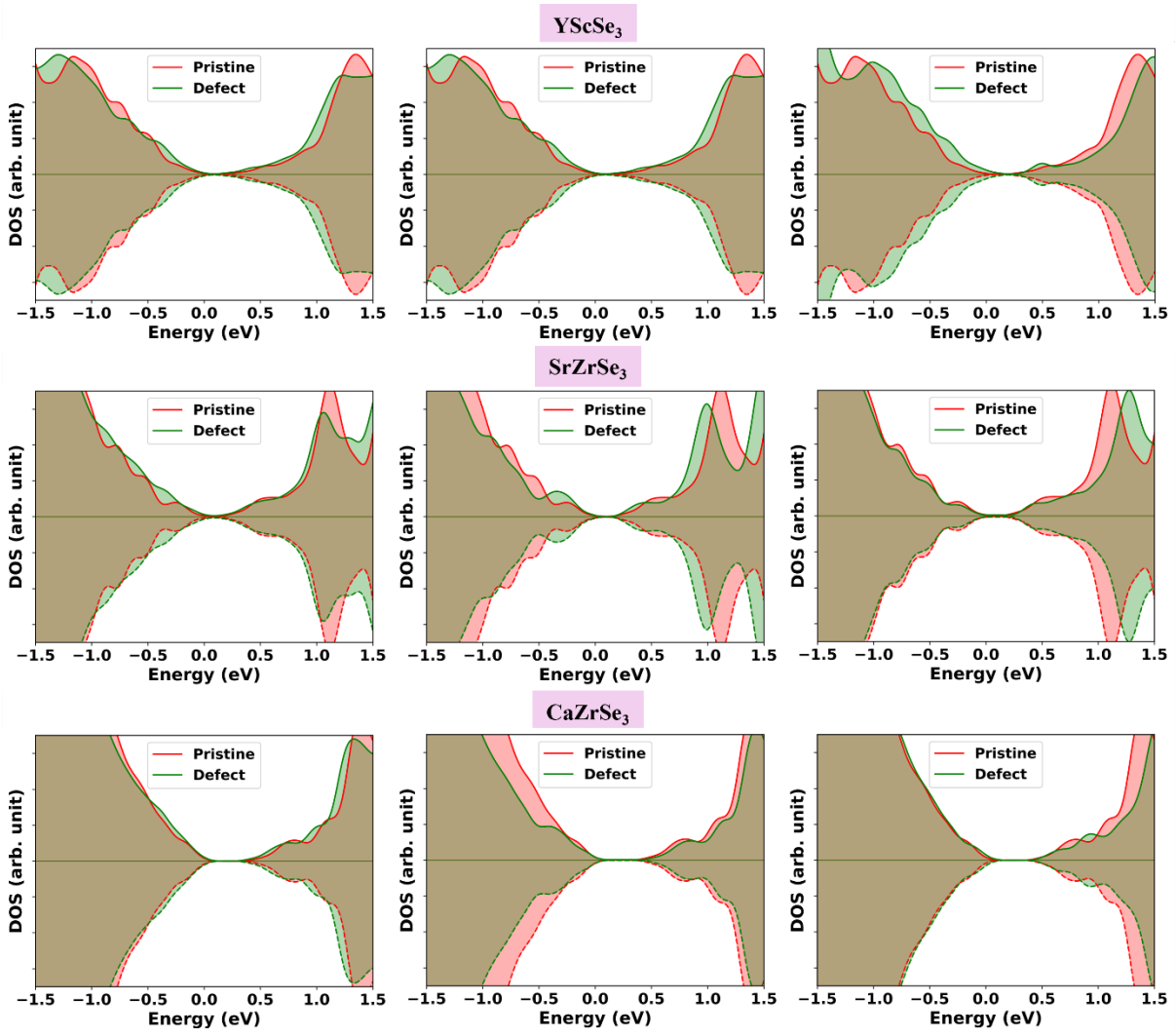
YScSe3
SrZrSe3
CaZrSe3
Pristine
Defect
DOS (arb. unit)
Energy (eV)
−1.5 −1.0 −0.5 0.0 0.5 1.0 1.5

Defect Intolerant DOS

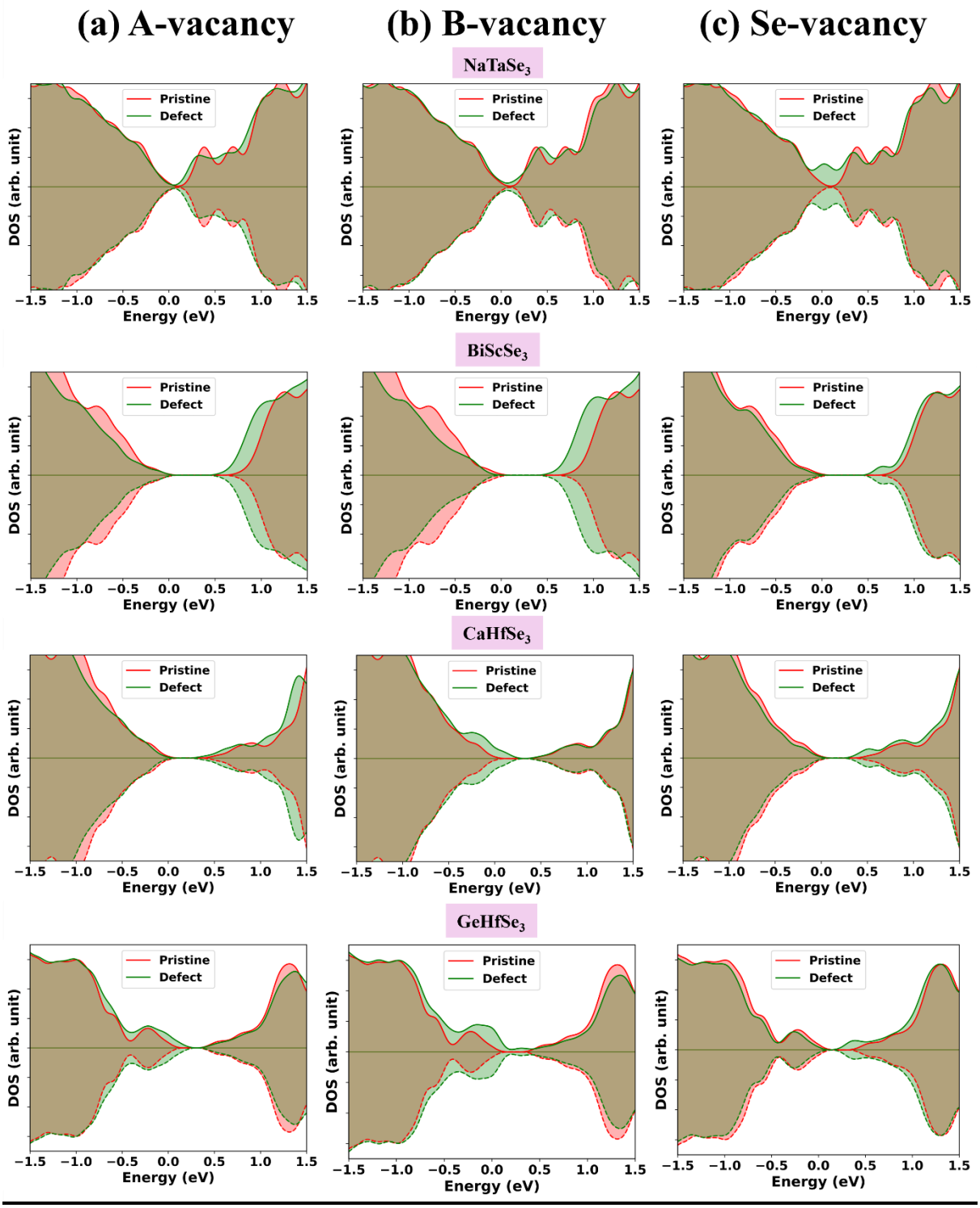

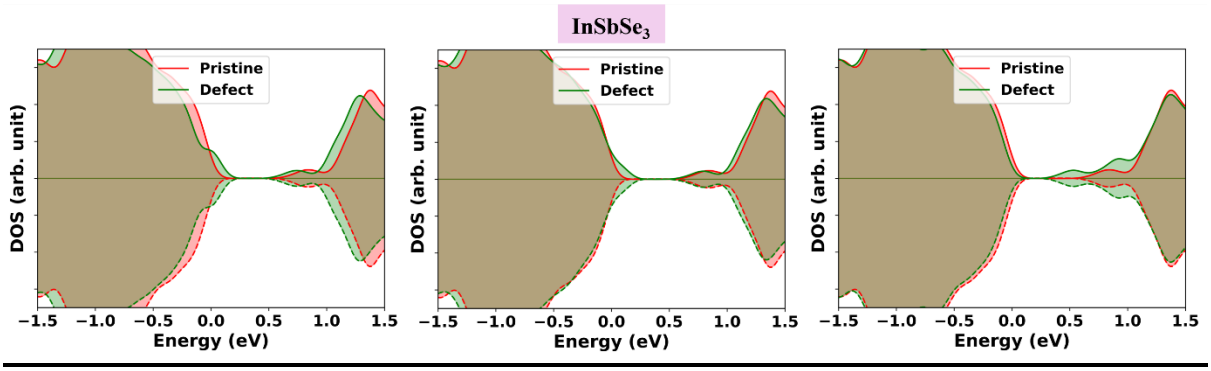

Figure S17: pDOS plots displaying the effect of (a) A cation vacancy, (b) M cation vacancy and (c) Se vacancy on screened AMSe3's.

(f) Thin-film Photovolatics:

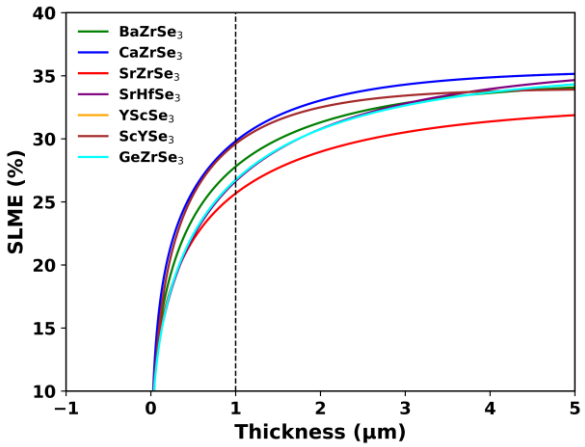

Figure S18: Thickness-dependent SLME of screened candidates.

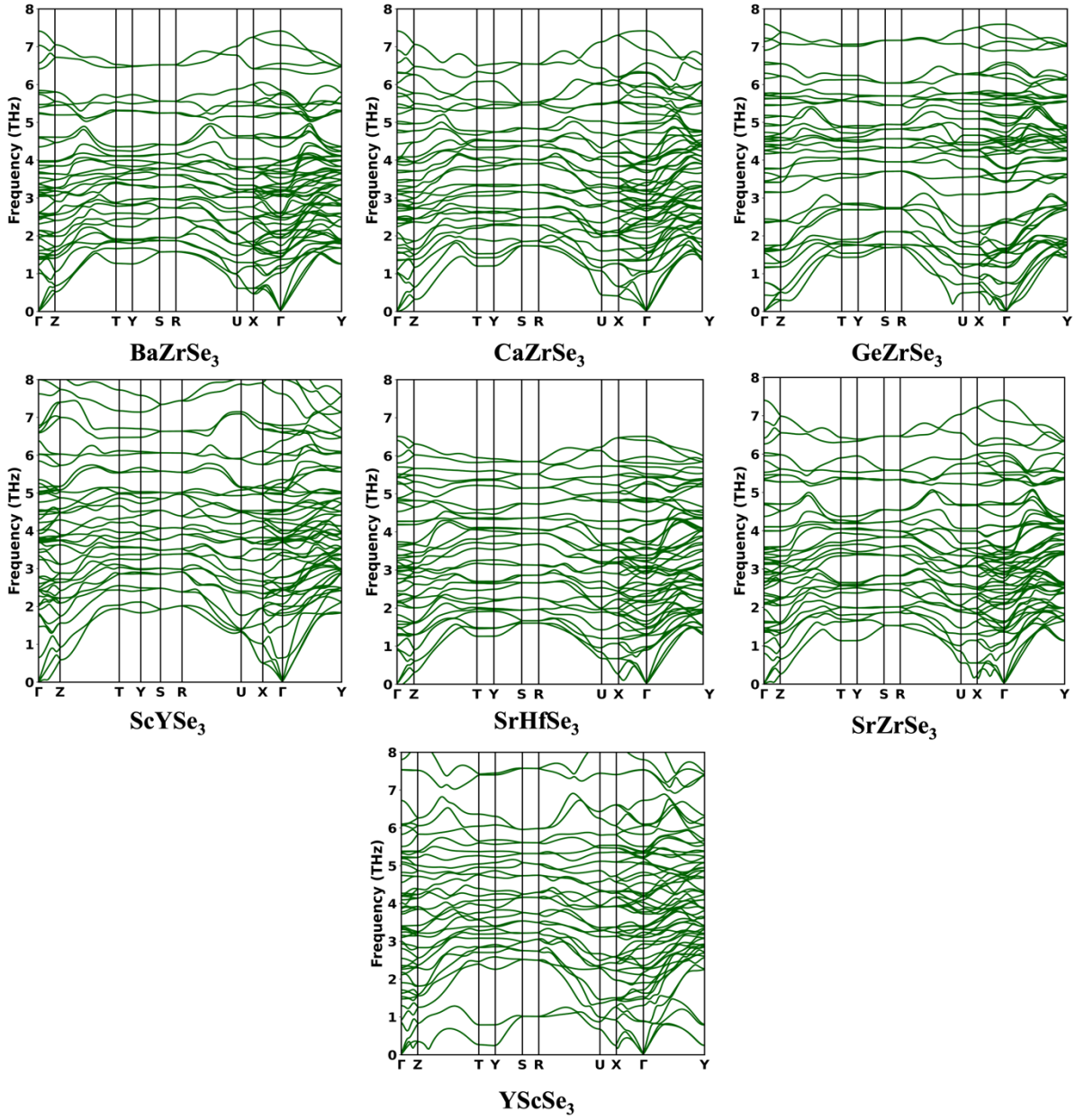

Figure S19: Phonon dispersions of screened candidates depicting the dynamical stability of these compounds due to the absence of any negative frequencies.

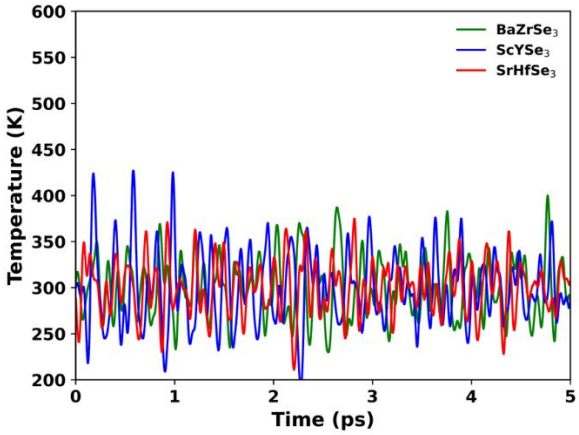

Figure S20: Temperature evolution over time during AIMD. These simulations are performed at 300 K.

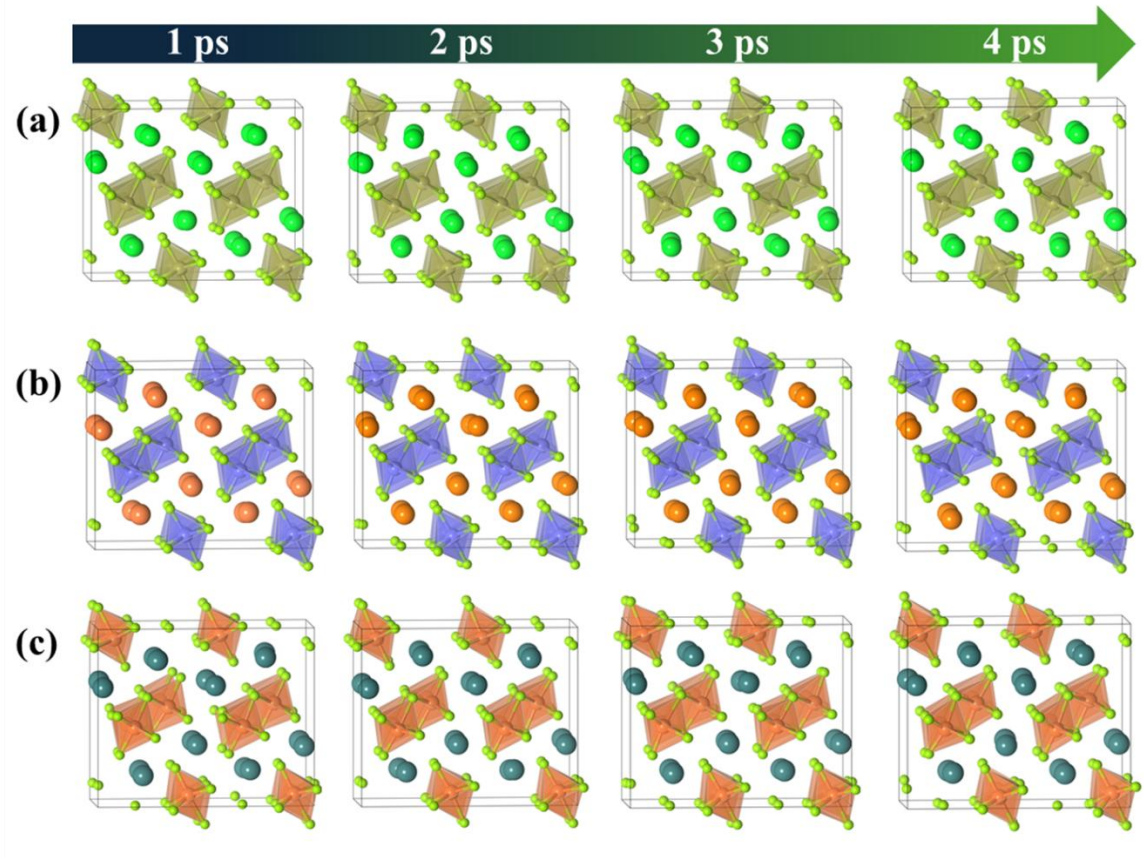

Figure S21: Structures of (a) $BaZrSe_3$, (b) $ScYSe_3$, and (c) $SrHfSe_3$ over time during AIMD.

Further reinforcing these findings, we tracked the temperature evolution over time, as depicted in Figure S18. The temperature profiles for $BaZrSe_3$, $ScYSe_3$, and $SrHfSe_3$ exhibit minimal fluctuations, which, in conjunction with the constrained energy oscillations, corroborate the

high thermal stability of these compounds. The convergence of both energy and temperature data provides compelling evidence that the $AMSe_3$ selenides can effectively maintain their structural integrity and stability under ambient conditions.

Section S8. Non Adiabatic Molecular Dynamics:

The carrier lifetimes of these materials are similar to that of inorganic halide perovskites and similar optoelectronic materials. Li et al. reported a non-radiative carrier lifetime of 1.45 ns for $CsPbBr_3$, which is one of the well-explored all-inorganic perovskite material and is known for its exceptional optoelectronic properties but is not suitable for practical use due to its lead toxicity.[27] Moreover, Zhao et al. reported a non-radiative carrier lifetime of 2.1 ns for $CsPbI_3$, which is comparable to our representative materials.

As observed from the time-averaged bandgap shown in Fig. 7(d), the bandgap value increases from 0.98 to 1.42 eV. This trend is in line with the inverse dependence of carrier lifetime on the bandgap values as described by Fermi's golden rule. Furthermore, the rate at which non-radiative recombination occurs is directly proportional to the square of the non-adiabatic coupling (NAC) strength. This strength indicates the probability of non-adiabatic transitions. The time-averaged NAC values indicated in Fig. 7d indicate the presence of faster recombination in the case of $BaZrSe_3$ and $SrHfSe_3$ than that of $ScYSe_3$. Primarily, these NAC values seem to have a relation with the bandgap values, which indicates that a smaller bandgap gives rise to stronger NAC coupling. The suitable band gap and decoupled electron-phonon dynamics in these ternary selenides result in a promisingly long carrier lifetime. We emphasize that all three materials have a relatively high non-radiative carrier lifetime, which is particularly important for potential optoelectronic applications.

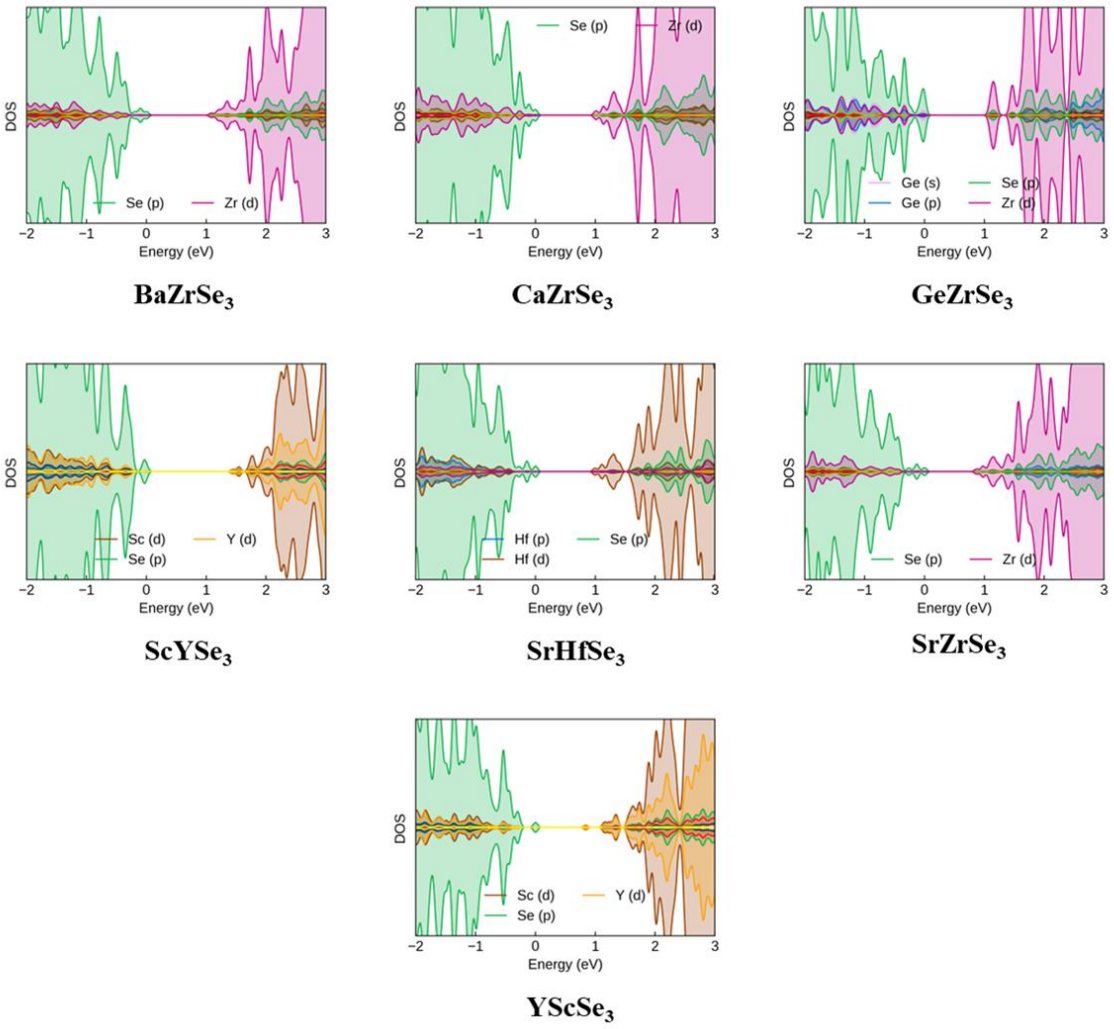

Figure S22: Partial DOS plots of final screened candidates.

Section S8: Descriptions of elemental features:

Features' Name (Abbreviation)	Description
min_mendeleev_number	Minimum mendeleev number*
min_electronegativity	Minimum electronegativity*
avg_electronegativity	Average electronegativity*

min_phi	Minimum work function*
max_ion_ener	Maximum ionization energy*
avg_ion_ener	Average ionization energy*
min_first_ionization_energy	Minimum first ionization energy*
Latt_b	Lattice parameter b
max_heat_fusion	Maximum heat fusion*
A_n_ws^third	Electron density at surface of Wigner-Sietz cell of A
Latt_c	Lattice parameter c
Latt_a	Lattice parameter a
A_Se_bond_distance	The bond distance between A and Se in the ASe bulk system
avg_LUMO	Average LUMO*
A_phi	Workfunction of A
min_electron_affinity	Minimum electron affinity*
max_MeltingT	Maximum melting temperature*
max_phi	Maximum work function*
E_hull	Energy above hull
E_form	Formation energy
avg_ZungerPP_r-pi	Average Zunger pseudopotential radius*

min_MV	Minimum molar volume*
avg_space_group_number	Average space group number*
moDiff_ion_ener	Modulus of the difference of the ionization energy *
max_n_ws^third	Maximum electron density at the surface of Wigner-Sietz cell*

Note: The '*' sign refers here to the value of all properties chosen between A and M.

References:

(1) Ong, S. P.; Richards, W. D.; Jain, A.; Hautier, G.; Kocher, M.; Cholia, S.; Gunter, D.; Chevrier, V. L.; Persson, K. A.; Ceder, G. Python Materials Genomics (Pymatgen): A Robust, Open-Source Python Library for Materials Analysis. *Comput Mater Sci* **2013**, *68*, 314–319. https://doi.org/10.1016/j.commatsci.2012.10.028.

(2) Jain, A.; Ong, S. P.; Hautier, G.; Chen, W.; Richards, W. D.; Dacek, S.; Cholia, S.; Gunter, D.; Skinner, D.; Ceder, G.; Persson, K. A. Commentary: The Materials Project: A Materials Genome Approach to Accelerating Materials Innovation. *APL Mater* **2013**, *1* (1). https://doi.org/10.1063/1.4812323.

(3) Jain, M.; Chelikowsky, J. R.; Louie, S. G. Reliability of Hybrid Functionals in Predicting Band Gaps. *Phys Rev Lett* **2011**, *107* (21), 216806. https://doi.org/10.1103/PhysRevLett.107.216806.

(4) Yu, L.; Zunger, A. Identification of Potential Photovoltaic Absorbers Based on First-Principles Spectroscopic Screening of Materials. *Phys Rev Lett* **2012**, *108* (6), 068701. https://doi.org/10.1103/PhysRevLett.108.068701.

(5) Togo, A.; Chaput, L.; Tadano, T.; Tanaka, I. Implementation Strategies in Phonopy and Phono3py. *Journal of Physics: Condensed Matter* **2023**, *35* (35), 353001. https://doi.org/10.1088/1361-648X/acd831.

(6) Tully, J. C. Molecular Dynamics with Electronic Transitions. *J Chem Phys* **1990**, *93* (2), 1061–1071. https://doi.org/10.1063/1.459170.

(7) Bittner, E. R.; Rossky, P. J. Quantum Decoherence in Mixed Quantum-Classical Systems: Nonadiabatic Processes. *J Chem Phys* **1995**, *103* (18), 8130–8143. https://doi.org/10.1063/1.470177.

(8) Akimov, A. V. Libra: An Open-Source "Methodology Discovery" Library for Quantum and Classical Dynamics Simulations. *J Comput Chem* **2016**, *37* (17), 1626–1649. https://doi.org/10.1002/jcc.24367.

(9) Ward, L.; Agrawal, A.; Choudhary, A.; Wolverton, C. A General-Purpose Machine Learning Framework for Predicting Properties of Inorganic Materials. *NPJ Comput Mater* **2016**, *2* (1), 16028. https://doi.org/10.1038/npjcompumats.2016.28.

(10) Guyon, I.; Weston, J.; Barnhill, S.; Vapnik, V. Gene Selection for Cancer Classification Using Support Vector Machines. *Mach Learn* **2002**, *46* (1/3), 389–422. https://doi.org/10.1023/A:1012487302797.

(11) Ong, M.; Guzman, D. M.; Campbell, Q.; Dabo, I.; Jishi, R. A. BaZrSe3: *Ab Initio* Study of Anion Substitution for Bandgap Tuning in a Chalcogenide Material. *J Appl Phys* **2019**, *125* (23). https://doi.org/10.1063/1.5097940.

(12) Tranchitella, L. J.; Chen, B.-H.; Fettinger, J. C.; Eichhorn, B. W. Structural Evolutions in the Sr1−Ba ZrSe3Series. *J Solid State Chem* **1997**, *130* (1), 20–27. https://doi.org/10.1006/jssc.1996.7253.

(13) Moroz, N. A.; Bauer, C.; Williams, L.; Olvera, A.; Casamento, J.; Page, A. A.; Bailey, T. P.; Weiland, A.; Stoyko, S. S.; Kioupakis, E.; Uher, C.; Aitken, J. A.; Poudeu, P. F. P. Insights on the Synthesis, Crystal and Electronic Structures, and Optical and Thermoelectric Properties of $Sr_{1-x}Sb_xHfSe_3$ Orthorhombic Perovskite. *Inorg Chem* **2018**, *57* (12), 7402–7411. https://doi.org/10.1021/acs.inorgchem.8b01038.

(14) Aykol, M.; Dwaraknath, S. S.; Sun, W.; Persson, K. A. Thermodynamic Limit for Synthesis of Metastable Inorganic Materials. *Sci Adv* **2018**, *4* (4). https://doi.org/10.1126/sciadv.aaq0148.

(15) Opahle, I.; Parma, A.; McEniry, E. J.; Drautz, R.; Madsen, G. K. H. High-Throughput Study of the Structural Stability and Thermoelectric Properties of Transition Metal Silicides. *New J Phys* **2013**, *15* (10), 105010. https://doi.org/10.1088/1367-2630/15/10/105010.

(16) Singh, H. K.; Zhang, Z.; Opahle, I.; Ohmer, D.; Yao, Y.; Zhang, H. High-Throughput Screening of Magnetic Antiperovskites. *Chemistry of Materials* **2018**, *30* (20), 6983–6991. https://doi.org/10.1021/acs.chemmater.8b01618.

(17) Sun, W.; Bartel, C. J.; Arca, E.; Bauers, S. R.; Matthews, B.; Orvañanos, B.; Chen, B.-R.; Toney, M. F.; Schelhas, L. T.; Tumas, W.; Tate, J.; Zakutayev, A.; Lany, S.; Holder, A. M.; Ceder, G. A Map of the Inorganic Ternary Metal Nitrides. *Nat Mater* **2019**, *18* (7), 732–739. https://doi.org/10.1038/s41563-019-0396-2.

(18) Du, Z.; Chen, X.; Hu, W.; Chuang, C.; Xie, S.; Hu, A.; Yan, W.; Kong, X.; Wu, X.; Ji, H.; Wan, L.-J. Cobalt in Nitrogen-Doped Graphene as Single-Atom Catalyst for High-Sulfur Content Lithium–Sulfur Batteries. *J Am Chem Soc* **2019**, *141* (9), 3977–3985. https://doi.org/10.1021/jacs.8b12973.

(19) Jiang, K.; Siahrostami, S.; Zheng, T.; Hu, Y.; Hwang, S.; Stavitski, E.; Peng, Y.; Dynes, J.; Gangisetty, M.; Su, D.; Attenkofer, K.; Wang, H. Isolated Ni Single Atoms in Graphene Nanosheets for High-Performance CO_2 Reduction. *Energy Environ Sci* **2018**, *11* (4), 893–903. https://doi.org/10.1039/C7EE03245E.

(20) Tian, H.; Tian, H.; Wang, S.; Chen, S.; Zhang, F.; Song, L.; Liu, H.; Liu, J.; Wang, G. High-Power Lithium–Selenium Batteries Enabled by Atomic Cobalt Electrocatalyst in Hollow Carbon Cathode. *Nat Commun* **2020**, *11* (1), 5025. https://doi.org/10.1038/s41467-020-18820-y.

(21) Feng, J.; Chen, D.; Pikhitsa, P. V.; Jung, Y.; Yang, J.; Choi, M. Unconventional Alloys Confined in Nanoparticles: Building Blocks for New Matter. *Matter* **2020**, *3* (5), 1646–1663. https://doi.org/10.1016/j.matt.2020.07.027.

(22) Chen, C.; Wu, D.; Li, Z.; Zhang, R.; Kuai, C.; Zhao, X.; Dong, C.; Qiao, S.; Liu, H.; Du, X. Ruthenium-Based Single-Atom Alloy with High Electrocatalytic Activity for Hydrogen Evolution. *Adv Energy Mater* **2019**, *9* (20). https://doi.org/10.1002/aenm.201803913.

(23) Yao, Y.; Huang, Z.; Xie, P.; Lacey, S. D.; Jacob, R. J.; Xie, H.; Chen, F.; Nie, A.; Pu, T.; Rehwoldt, M.; Yu, D.; Zachariah, M. R.; Wang, C.; Shahbazian-Yassar, R.; Li, J.; Hu, L. Carbothermal Shock Synthesis of High-Entropy-Alloy Nanoparticles. *Science (1979)* **2018**, *359* (6383), 1489–1494. https://doi.org/10.1126/science.aan5412.

(24) Yao, Y.; Huang, Z.; Li, T.; Wang, H.; Liu, Y.; Stein, H. S.; Mao, Y.; Gao, J.; Jiao, M.; Dong, Q.; Dai, J.; Xie, P.; Xie, H.; Lacey, S. D.; Takeuchi, I.; Gregoire, J. M.; Jiang, R.; Wang, C.; Taylor, A. D.; Shahbazian-Yassar, R.; Hu, L. High-Throughput, Combinatorial Synthesis of Multimetallic Nanoclusters. *Proceedings of the National Academy of Sciences* **2020**, *117* (12), 6316–6322. https://doi.org/10.1073/pnas.1903721117.

(25) Moroz, N. A.; Bauer, C.; Williams, L.; Olvera, A.; Casamento, J.; Page, A. A.; Bailey, T. P.; Weiland, A.; Stoyko, S. S.; Kioupakis, E.; Uher, C.; Aitken, J. A.; Poudeu, P. F. P. Insights on the Synthesis, Crystal and Electronic Structures, and Optical and Thermoelectric Properties of $Sr_{1-x}Sb_xHfSe_3$ Orthorhombic Perovskite. *Inorg Chem* **2018**, *57* (12), 7402–7411. https://doi.org/10.1021/acs.inorgchem.8b01038.

(26) Adhikari, S.; Johari, P. Photovoltaic Properties of <math> <mrow> <mi>A</Mi> <mi>B</Mi> </Mrow> <msub> <mi Mathvariant="normal">Se</Mi> <mn>3</Mn> </Msub> </Math> Chalcogenide Perovskites (<math> <mi>A</Mi> </Math> = Ca, Sr, Ba; <math> <mi>B</Mi> </Math> = Zr, Hf). *Phys Rev B* **2024**, *109* (17), 174114. https://doi.org/10.1103/PhysRevB.109.174114.

(27) Li, W.; Vasenko, A. S.; Tang, J.; Prezhdo, O. V. Anharmonicity Extends Carrier Lifetimes in Lead Halide Perovskites at Elevated Temperatures. *J Phys Chem Lett* **2019**, *10* (20), 6219–6226. https://doi.org/10.1021/acs.jpclett.9b02553.